Aerodynamic Design Optimization of a Transonic Strut-Braced-Wing Regional Aircraft

Timothy Chau* and David W. Zingg†
Institute for Aerospace Studies, University of Toronto, ON M3H 5T6

The aerodynamic design and fuel burn performance of a Mach 0.78 strut-braced-wing regional jet is investigated through aerodynamic shape optimization based on the Reynolds-averaged Navier-Stokes equations. Conceptual-level multidisciplinary design optimization is first performed to size the strut-braced-wing aircraft for a design mission similar to the Embraer E190-E2, with a design range of 3,100 nmi at a maximum capacity of 104 passengers, and a maximum payload of 30,200 lb. For direct performance comparisons, a conventional tube-and-wing regional jet is also sized and optimized based on the same reference aircraft. Gradient-based aerodynamic shape optimization is then performed on wing-body-tail models of each aircraft, with the objective of drag minimization at cruise over a 500 nmi nominal mission. Design variables include twist and section shape degrees of freedom, which are realized through a free-form and axial deformation geometry control system, while nonlinear constraints include constant lift, zero pitching moment, minimum wing volume, and minimum maximum thickness-to-chord ratios. Results indicate that the optimizer is capable of mitigating shock formation, boundary-layer separation, and other flow interference effects from each wing design, including those within the wing-strut junction of the strut-braced wing. With year 2020 technology levels, the strut-braced-wing regional jet offers a 12.9% improvement in cruise lift-to-drag ratio over an Embraer E190-E2-like conventional tube-and-wing aircraft, which translates to a 7.6% reduction in block fuel for the nominal mission.

Nomenclature

α = Angle of attack

b = Span

C_D = Drag coefficient

C_L = Lift coefficient

C_M = Pitching moment coefficient

*Ph.D. Candidate, Institute for Aerospace Studies, University of Toronto, AIAA Student Member, tim.chau@mail.utoronto.ca

†Distinguished Professor of Computational Aerodynamics and Sustainable Aviation, Institute for Aerospace Studies, University of Toronto, Associate Fellow AIAA, dwz@utias.utoronto.ca

C_P = Pressure coefficient

c = Chord

D = Drag

L = Lift

L/D = Lift-to-drag ratio

M = Mach number

N = Number of grid nodes

S_{ref} = Reference area (gross)

T = Maximum thrust, SLS

t/c = Thickness-to-chord ratio

x,y,z = Cartesian coordinates

y^+ = Nondimensional off-wall distance

Acronyms

CG = Center of Gravity

CTW = Conventional Tube-and-Wing

FFD = Free-Form Deformation

ICA = Initial Cruise Altitude

MAC = Mean Aerodynamic Chord

MDO = Multidisciplinary Design Optimization

MFW = Maximum Fuel Weight

MTOW = Maximum Takeoff Weight

MZFW = Maximum Zero Fuel Weight

NR = Nominal Range

OEW = Operating Empty Weight

OML = Outer Mold Line

RANS = Reynolds-Averaged Navier-Stokes

SBW = Strut-Braced Wing

SNOPT = Sparse Nonlinear OPTimizer

TSFC = Thrust Specific Fuel Consumption

I. Introduction

With concerns over the environmental impact of commercial aviation on the rise, novel aircraft configurations have become of significant interest to the aviation industry due to their high potential for reducing fuel burn and emissions relative to the conventional tube-and-wing. Some examples in consideration today include the blended or hybrid wing-body [1], the joined and box wings [2–5], and the D8 [6], each exhibiting unique advantages enabled by their unconventional airframe designs. Another concept of interest is the truss-braced wing, which is particularly attractive because of its high potential for near-term entry into service.

The primary advantage of the truss-braced-wing configuration comes from having a much larger wing span, typically with aspect ratios ranging from 16-20 as compared to 9-11 for current conventional wings, which allows it to benefit from significant reductions in induced drag, while in principle remaining compatible with conventional fuselage and empennage designs. Normally, such long and slender wings lead to large wing-bending loads that are impractical due to dramatic penalties in structural weight. The truss-braced-wing configuration, however, features a structurally-efficient truss topology, consisting of a main strut and one or more jury struts, which can not only mitigate these penalties, but in principle, can offer a surplus in weight savings. This structural efficiency can be leveraged to enable thinner wing sections, leading to lower form drag and reduced susceptibility to wave drag. As a result of the latter, a further reduction in structural weight can be achieved by lowering the sweep angle of the wings; this would also open the possibility for extending the laminar flow region over the wing, further reducing drag. A variant of the truss-braced-wing configuration is the strut-braced wing, which includes only the main strut to trade structural efficiency for higher aerodynamic performance by virtue of lower wetted area and reduced interference effects.

Pfenninger [7] has been credited with first conceiving the benefits of the strut- and truss-braced wing configurations for long-range, transonic transport aircraft in 1954. Since then, a number of studies have been performed using multidisciplinary design optimization (MDO), given the strong coupling between the aerodynamic and structural design of the configuration. Studies done by Grasmeyer et al. [8] and Gern et al. [9], for example, investigated the conceptual design of a wide-body strut-braced-wing transport aircraft by applying a low-fidelity MDO environment. Gur et al. [10] extended this framework to encompass both strut- and truss-braced wings. Meadows et al. [11] and Chakraborty et al. [12] then applied it to the study of single-aisle strut- and truss-braced-wing transport aircraft. Owing to the promising fuel savings indicated by these studies, NASA and Boeing investigated a Mach 0.70 truss-braced-wing single-aisle aircraft similar to the Boeing 737-800 [13]. With advanced technologies such as natural laminar flow and next-generation propulsion systems, this concept, known as the Boeing SUGAR High, projected a 53.6-56.0% savings in block fuel per seat over a 900 nmi mission when compared to a conventional aircraft configuration with current technologies.

Concerns from the airline industry over the loss of productivity when operating at lower Mach numbers, however, have given rise to the need for investigating strut- and truss-braced-wing configurations at more conventional Mach

numbers. NASA and Boeing have since transitioned to exploring transonic truss-braced-wing aircraft concepts for Mach 0.745 [14] and Mach 0.80 [15, 16], with current efforts focused on the latter.

While the above studies have demonstrated the potential benefits of strut- and truss-braced wings, there remains motivation for further investigations into a number of challenges that can only be addressed through high-fidelity simulation tools. One critical issue is the aerodynamic design of the enclosed regions formed by the wing, strut(s), and fuselage, which emulate transonic channels. These can cause the flow to accelerate and form shock waves, even at moderate Mach numbers, potentially leading to boundary-layer separation and severe drag penalties. Such an obstacle is made even more difficult to overcome at high transonic Mach numbers, which places it at odds with airline productivity.

Some work has been done in an attempt to address this issue. Ko, Mason, and Grossman [17], for instance, investigated the aerodynamic design of a wing-strut junction for a Mach 0.85 fighter jet through an Euler-based cut-and-try approach. By modeling a region of the flow within the junction as a transonic nozzle, it was found that incorporating a flattened upper surface strut can reduce the effective area ratio below the critical value, weakening the shock, and in some cases preventing its formation. It remains unclear, however, whether such a feature is aerodynamically optimal in terms of lift and drag, and if not, whether some other form of area ruling can provide further improvements.

More recently, the Platform for Aircraft Drag Reduction Innovation (PADRI) workshop [18] provided participants with a common strut-braced-wing aircraft geometry to explore various avenues for shock elimination within the wing-strut junction. Included were a range of aerodynamic design and optimization strategies, and flow control techniques, with some strategies showing success. The PADRI concept, however, was designed for a relatively low Mach-C_L combination at 0.70 and 0.4057, respectively, leaving many open questions at higher Mach numbers and lift coefficients.

Meanwhile, there remains the challenge of achieving and maintaining a favorable tradeoff between lower induced drag and higher viscous drag when adopting a high aspect ratio wing design with a similar wing area, and when introducing strut members. Often, part of the solution is to operate at much higher lift coefficients, which demands flight at higher cruise altitudes (see for example Ref. [19]). At a fixed wing loading, this leads to a re-balancing of the parasite and induced drag components, resulting in more optimal lift-to-drag ratios. This comes with a number of system level consequences, however, including increased fuel requirements for the climb and descent segments, weight penalties associated with elevated cabin pressurization loads, and larger propulsion systems. Moreover, operating at high lift coefficients can exacerbate susceptibility to wave drag.

One approach to addressing these challenges is through high-fidelity aerodynamic shape optimization, which automates the aerodynamic design based on simulations of the flow physics. Such methods are well-suited for investigating unconventional aircraft configurations given that prior design experience and knowledge surrounding these concepts is often limited. For instance, in the work of Gagnon and Zingg [20], Euler-based aerodynamic shape

optimization was applied to the aerodynamic design of a Mach 0.78 strut-braced-wing regional jet. Here, the shocks within the wing-strut junction were removed, maintaining a favorable lift-to-drag ratio when compared to an equivalent conventional tube-and-wing aircraft. Given the inviscid nature of the Euler equations, however, this work could not account for the tradeoffs between induced drag and viscous drag.

Trade-offs between induced drag and viscous drag can be addressed through the Reynolds-averaged Navier-Stokes (RANS) equations, which can also capture shock formation and boundary-layer separation. In a study done by Secco and Martins [21], RANS-based aerodynamic shape optimization was shown to be effective at removing shocks within the wing-strut junction of the PADRI geometry, while maintaining a lift-to-drag ratio exceeding 20 for the wing-strut-fuselage model. Given the modest operating conditions of the PADRI concept, however, the question remains whether the presence of shocks can be mitigated when considering more conventional transonic Mach numbers and higher lift coefficients.

Assuming that a low drag design can be achieved at these more demanding flight conditions, not only at the design point, but also over a range of suitable operating conditions, the next challenge will be to assess the impact of these aerodynamic design features on the structural design of the wing system. Such an integrated design problem can prove to be difficult due to the competing aspects of each discipline, especially given both the flexible nature of the very thin and high aspect ratio wing, and the vulnerability of the joined-wing system to global buckling. In this regard, high-fidelity aerostructural optimization tools can aid in investigating this coupling, while also enabling aeroelastic tailoring. Examples include Brooks, Kenway, and Martins [22] and Khosravi and Zingg [23]. More recent work [24] has also demonstrated the suitability of such tools for investigating the aerostructural design and performance of high aspect ratio wings with advanced materials.

The final barrier for the strut- and truss-braced-wing configurations will likely be the susceptibility of the highly flexible wings to aeroelastic instabilities such as flutter at transonic flight conditions (see for example Bartels, Funk, and Scott [25]). Some recent work has shown that low-fidelity modeling can be useful for estimating the flutter boundary for conceptual-level problems [26, 27]. However, such methods can often lead to designs that are too conservative, in part because they are unable to accurately capture the nonlinear behavior of transonic aerodynamics, as well as the complex interactions between aerodynamics and structures present in joined wing systems. To address this issue, some researchers [28] are making progress towards developing flutter constraints for high-fidelity aerostructural optimization. Meanwhile, reduced order modeling can provide an excellent opportunity for lowering the cost of such constraints [29], which has already been used extensively in the field of aeroelastic analysis [30, 31].

Nonetheless, the first step in reducing the risk and uncertainty surrounding the viability of the strut- and truss-braced-wing configurations for transonic transport aircraft is to investigate the aerodynamic design challenges associated with their unconventional wing systems. Towards this end, the primary contribution of this paper is an application of RANS-based aerodynamic shape optimization to the aerodynamic design of a transonic strut-braced-wing regional jet,

with three main objectives:

1) To determine if a low drag strut-braced wing design can be achieved at Mach 0.78 when accounting for induced, viscous, and wave drag, as well as transonic interference effects in and around the wing-strut junction
2) To investigate aerodynamic design features and tradeoffs that are associated with such low drag strut-braced wings
3) To provide a credible estimate for the relative fuel savings offered by the strut-braced-wing configuration in the regional jet class

With regard to the third objective, a conventional tube-and-wing regional jet will also be optimized, serving as a performance baseline that represents a modern, best-in-class regional jet similar to the Embraer E190-E2. For the strut-braced wing, year 2020 technology levels will be assumed to avoid the uncertainty surrounding the benefits associated with advanced technologies and to focus on the potential fuel burn advantages of the configuration itself. In this way, the present study will aim to provide an understanding of how well the strut-braced-wing configuration can perform in the regional jet class with known technologies when compared to a competitive in-service conventional tube-and-wing.

The paper is organized as follows. Section II provides an overview of the high-fidelity aerodynamic shape optimization framework, as well as an overview of a mixed low- and medium-fidelity MDO environment that is used to perform the conceptual design of each aircraft. Section III describes each conceptual design problem and includes the results for each aircraft, while Section IV presents the problem formulations and results for the high-fidelity aerodynamic shape optimizations. Conclusions are presented in Section V.

II. Methodology

A. High-Fidelity Aerodynamic Shape Optimization Framework

Aerodynamic design optimization is performed through a high-fidelity aerodynamic shape optimization framework called `Jetstream` that has been developed at the University of Toronto Institute for Aerospace Studies. It consists of an integrated geometry parameterization and mesh-deformation scheme [32], a free-form and axial deformation geometry control system [33], a Newton-Krylov-Schur flow solver for the RANS equations fully coupled with the Spalart-Allmaras turbulence model [34], the discrete-adjoint method [35, 36] for flow- and mesh-dependent gradient evaluation, and `SNOPT` [37] for gradient-based optimization. Together, these components provide an automated approach to aerodynamic design that is driven by accurate simulations of the flow physics.

1. Integrated Geometry Parameterization and Mesh Deformation

Each block of a structured multiblock grid is first parameterized with B-spline volumes, which projects the computational mesh onto a space in which the analytical surface definition is maintained throughout the optimization.

In this work, cubic B-spline volumes are used, while knot vectors are defined with an equal number of computational mesh nodes within each interval, allowing the control grid to mimic the spatial distribution of nodes on the CFD grid. This ensures that more control is placed near regions of higher curvature and regions where high mesh resolution and quality is important, such as in the boundary layer.

For mesh deformation, each B-spline volume is modeled as a linear elastic solid where deformations applied to the subset of control points defining the aerodynamic surfaces are propagated throughout the control grid of each of these blocks, as well as all other blocks within the computational domain. This allows each block to be regenerated algebraically in parallel, providing an update to the entire computational mesh. In order to preserve the quality of the computational mesh, the stiffness of each element is defined to be proportional to its volume and a measure of its orthogonality [32]. In addition to maintaining a smooth representation of the aerodynamic surfaces, the integrated mesh deformation scheme is also capable of achieving large shape changes. This can be accomplished by subdividing the mesh update into increments of smaller linear elastic changes, thus maintaining the quality of the mesh. Since the control grid typically has 2-3 orders of magnitude fewer nodes than the computational mesh, the integrated mesh deformation strategy can perform mesh updates at a small fraction of the cost of a flow analysis.

2. Geometry Control

Geometry control is provided by the free-form and axial deformation method, where local shape control is provided by free-form deformation (FFD) volumes, and global shape control is provided by axial curves that drive these FFD volumes. The FFD volumes are defined as B-spline volume lattices that transform an embedded object of interest as the FFD volumes themselves are deformed. In this way, the shape deformation process is dissociated from the shape representation of the embedded object, allowing for the use of fewer yet more intuitive design variables. As with Gagnon and Zingg [33], the B-spline control points that define the aerodynamic surfaces are embedded within the FFD volumes, as opposed to the surface mesh nodes. This ensures that the analytical representation of the aerodynamic surfaces is maintained by virtue of the B-spline parameterization.

Although the x-, y-, and z-coordinates of the FFD volumes can be used as design variables, these primitive degrees of freedom are instead translated to more practical design variables through the use of rotation and scaling operators. In particular, the design variables are section shape degrees of freedom plus twist and taper, which for a given FFD-volume cross-section are defined as follows:

- **Twist:** a rotation of the FFD-volume cross-section in the local xz-plane about the local origin
- **Taper:** a uniform scaling of the FFD-volume cross-section in the local xz-plane with respect to the local origin
- **Section Shape:** a scaling of the vertical distance from the local origin to the position of a given FFD-volume control point along the local z-axis; this design variable is defined separately for each individual FFD-volume control point

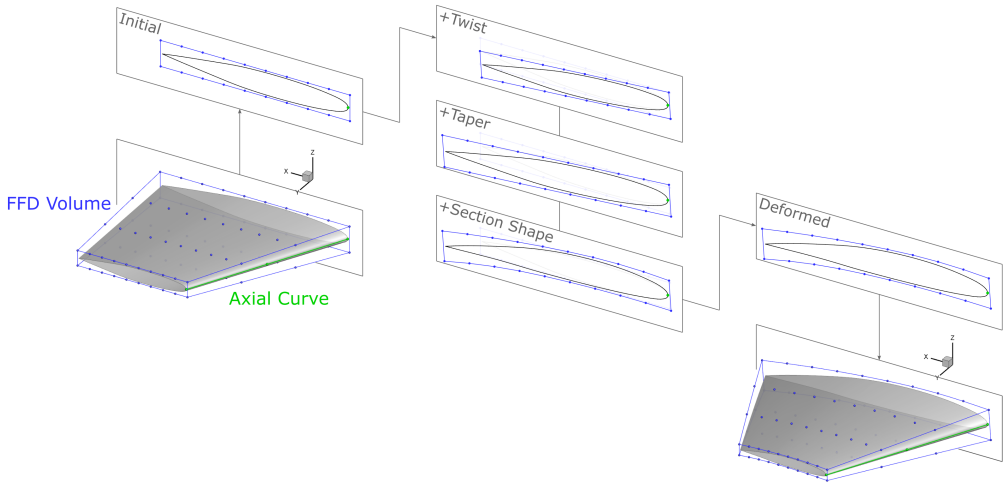

Fig. 1 Notional diagram of the free-form and axial deformation geometry control system. Local shape control is shown through twist, taper, and section shape deformations applied across the FFD volume, with the shape changes at the root highlighted.

These transformation operators are applied in sequence to the initial xyz-coordinates of the FFD-volume lattice at each update, with changes following a cubic interpolation between FFD-volume control points in the parametric chordwise direction, a cubic interpolation between each FFD-volume cross-section in the parametric spanwise direction, and a linear interpolation between each chordwise pair of control points of a given FFD-volume cross-section in the parametric vertical direction. These correspond to the order of the B-spline volume along each parametric direction. Figure 1 illustrates an example setup of the free-form and axial deformation geometry control system for a wing segment, and demonstrates how each FFD design variable is applied to a given FFD-volume cross-section in sequence.

The axial curve, defined as a B-spline curve, is threaded through the local origin of each FFD-volume cross-section, which is often positioned at the leading edge, quarter chord, or trailing edge of the wing object. Since the FFD-volume cross-sections must remain attached and normal to the axial curve based on their initial parametric positions, the axial curves can be manipulated to produce global changes to the embedded object. In particular, these design variables are called sweep, span, and dihedral degrees of freedom, and are defined as follows:

- **Sweep:** a translation in the x-coordinate of a given axial curve control point
- **Span:** a translation in the y-coordinate of a given axial curve control point
- **Dihedral:** a translation in the z-coordinate of a given axial curve control point

Figure 2 demonstrates how these degrees of freedom can be used to provide global shape control when applied to a wing segment. Figure 3 illustrates the relationship between the geometry control system and the integrated geometry parameterization and mesh-deformation algorithm.

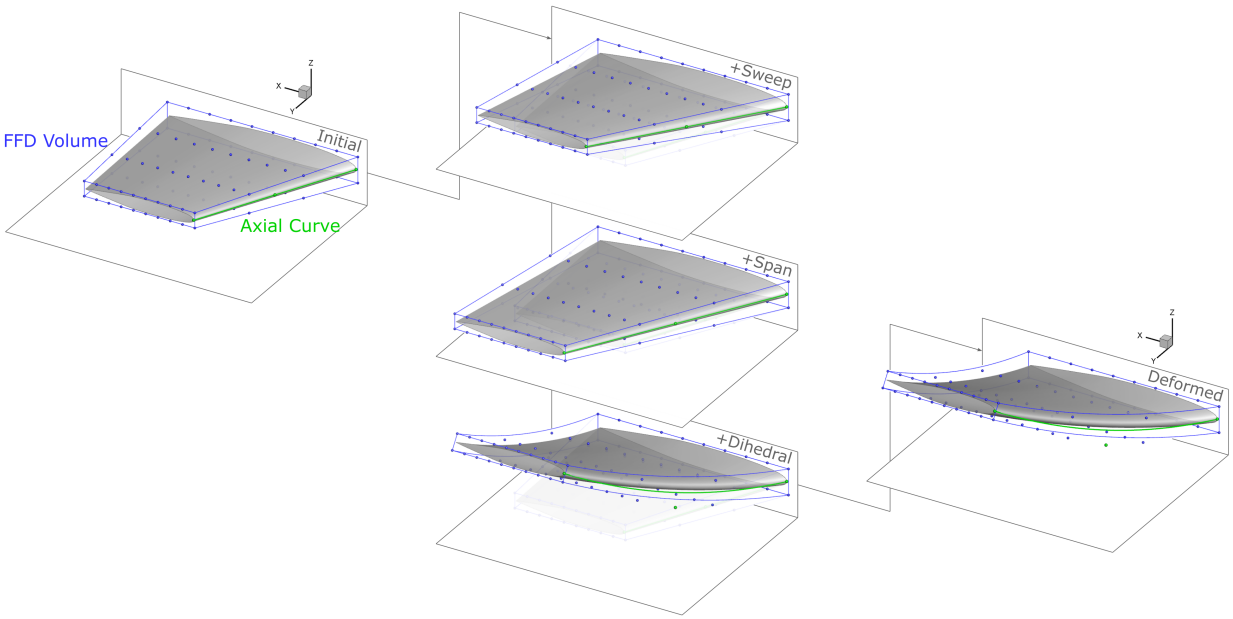

Fig. 2 Notional diagram of the free-form and axial deformation geometry control system. Global shape control is shown through sweep, span, and dihedral deformations applied in sequence to an axial curve located at the leading edge of a wing segment.

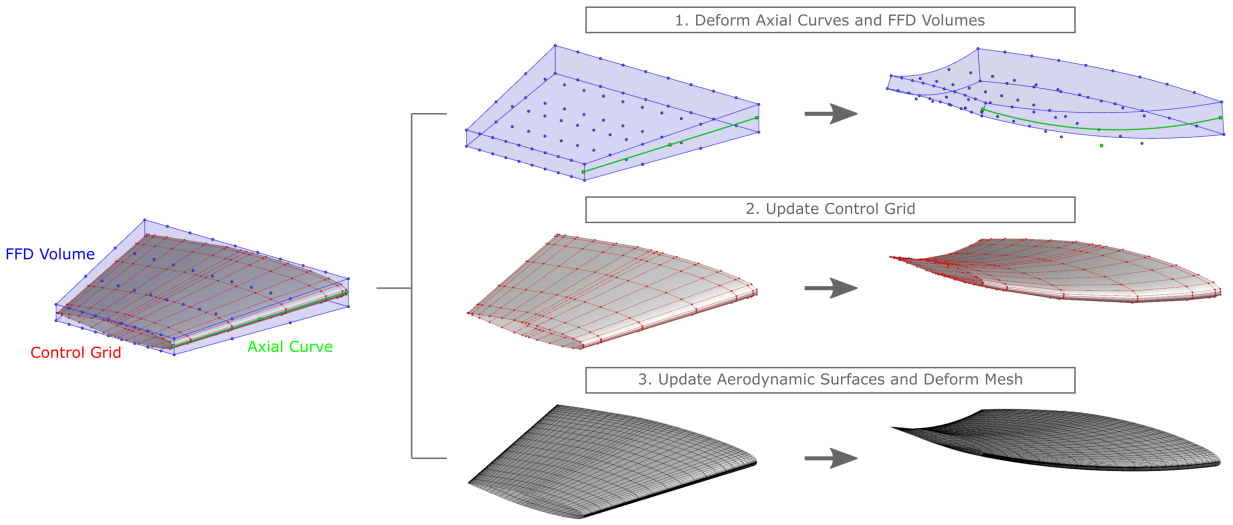

Fig. 3 Control sequence for deforming the geometry and mesh starting from the free-form and axial deformation geometry control system.

3. Flow Solver

Aerodynamic functionals are computed through a three-dimensional structured multiblock flow solver for the RANS equations fully coupled with the Spalart-Allmaras (SA) turbulence model [38]. Specifically, the SA-neg model [39] is used in conjunction with QCR2000 [40], the latter of which has been shown to aid in properly resolving flow separation

in and around junction regions [41]. For spatial discretization, second-order centered difference summation-by-parts (SBP) operators [42] are used with simultaneous approximation terms (SATs) to enforce boundary conditions and couple block interfaces weakly. To stabilize shocks, a pressure sensor is used to control the activation of artificial dissipation. This comes in the form of 2nd- and 4th-difference scalar dissipation operators, although matrix dissipation is also available. Boundary layers are assumed to be fully turbulent, although `Jetstream` also has the capability for laminar-to-turbulent transition prediction [43].

The numerical solution to the system of nonlinear equations is computed using a parallel implicit Newton-Krylov algorithm with a form of pseudo-transient continuation for globalization. The linear system that arises during each Newton phase is solved inexactly using a flexible variant of the Krylov subspace method, generalized minimal residual (GMRES) [44, 45], and is subject to Schur preconditioning [46].

The flow solver has been validated against results from the Fifth Drag Prediction Workshop (DPW5) [41], with the drag coefficient of the NASA Common Research Model (CRM) predicted within one drag count of the median across all participants [47].

4. Gradient Evaluation and Optimization

Gradient-based optimization is performed by `SNOPT` [37], which is a numerical optimizer that can solve large-scale linear and nonlinear constrained optimization problems. For the evaluation of the objective function gradient, as well as constraint gradients that depend on the flow solution, the discrete-adjoint method is employed [35, 36]. For all other constraints, gradients are calculated either analytically or through the complex-step method [48]. For more details on the gradient calculations, see Osusky et al. [49].

B. Conceptual Design Environment

The conceptual design of each aircraft is performed with a mixed low- and medium-fidelity MDO environment called `Faber`, which has also been developed at the University of Toronto Institute for Aerospace Studies and is presented for the first time in the present paper. `Faber` provides a means for the systems-level analysis, sizing, and optimization of transport aircraft, with a focus on developing aircraft that are representative of a given configuration and class in order to support aerodynamic design investigations through the application of `Jetstream`. This is achieved through low-order models for several disciplinary analyses including (1) aerodynamics, (2) weight and balance, (3) structures, (4) propulsion, and (5) performance, which enables the capturing of interdisciplinary tradeoffs to first order. These modules are interfaced with a numerical optimizer that drives a given aircraft design towards a minimum fuel burn solution, while providing a means for incorporating top-level aircraft requirements in the form of linear and nonlinear constraints.

For drag estimation, the aerodynamics module includes profile drag (i.e. skin friction drag, form drag, interference

drag, and excrescence drag) from the wing, fuselage, horizontal and vertical tails, nacelles, and pylons, as well as induced drag and wave drag from the wing. Profile drag is calculated using the method of Raymer [50], which includes the Prandtl-Schlichting relation for turbulent flow, while induced drag is determined by a vortex lattice method coupled with a Trefftz-plane analysis, assuming elliptical lift distributions. For wave drag, the method of Malone and Mason [51] is used, which employs the Korn equation corrected for swept wings. Miscellaneous drag contributions such as fuselage upsweep drag are also included.

Wing weight estimation is performed using a semi-empirical approach that combines an equivalent beam model for calculating the primary weight of the wing structure with statistical correlations for secondary weights, which account for the wing ribs, minimum gauge structures (i.e. fixed leading and trailing edges), high-lift devices (i.e. slats, flaps, and spoilers), control systems (i.e. ailerons), support structures, and non-optimum structures [52]. These relations depend primarily on the maximum takeoff weight (MTOW) and, where applicable, the projected area of each component, obtained from the reference aircraft. This method provides the flexibility required to handle unconventional wing systems.

The equivalent beam model consists of a finite element method that assumes that the primary wing structure can be represented by a discrete number of two-node beam elements with six degrees of freedom per node (i.e. three displacements and three rotations), and an airfoil conforming wing box model that consists of six booms and skins [53]. Structural thicknesses (i.e. boom areas and skin thicknesses) are sized based on a fully-stressed criterion, which according to Gallman, Smith, and Kroo, is comparable to that of a design obtained from structural optimization [54]. As per Andrews, Perez, and Wowk [53], the booms are assumed to support only normal stresses from bending moments and axial forces, while the skins support shear stresses from torsional moments and shear forces. RAE-2822 airfoil profiles are used, which are representative of typical transonic airfoils in terms of their camber and thickness distributions. These sections are scaled to match the maximum thickness-to-chord ratios defined by the user, or as determined by the optimization framework.

Once the structural thicknesses have been sized for a given load condition, the finite element problem is solved via the matrix stiffness method [55, 56]. This procedure is carried out iteratively until the location of the center of gravity of each wing box cross-section has converged. The load conditions include $+2.5g$ and $-1g$ balanced maneuver loads. To ensure that wing segments under compression do not fail due to buckling, a nonuniform column buckling model based on Euler-Bernoulli beam theory is employed to detect global buckling. For wing spans that are greater than the gate limit (e.g. 118 ft for code C gates), a folding wing mechanism is assumed, with a weight penalty added based on a semi-empirical correlation provided by Gur et al. [57]. This model is based on the extent of the wing beyond the fold, and assumes an elliptical lift distribution.

Other weight contributions come from the fuselage, horizontal and vertical tails, nacelles and pylons, landing gear, propulsion system, aircraft systems, and operational items, which are assumed to be conventional. These weights are

approximated with the statistical correlations of Torenbeek [52], with their center of gravity locations determined by the statistical correlations of Kroo and Shevell [58].

Fuel weights are calculated with the method of fuel fractions [50], with the exception of the cruise segments, which are determined by the Breguet range equation. Fuel tanks are modeled between the fore and aft spars of each wing segment, and follow the OMLs used by the structures module. A utilization factor is applied to account for internal structures and trapped fuel. Advanced fuel schedules are not employed. Instead, the fuel is assumed to be distributed and consumed uniformly across each fuel tank. Based on these models, the volume centroids are used for the center of gravity location of the fuel weight and tanks.

In order to resize the propulsion system to satisfy the mission requirements over the operating envelope of the aircraft, `Faber` uses the rubber engine model of Gur et al. [57]. These statistical correlations provide a means for adjusting the propulsion system weight, nacelle and pylon drag, thrust specific fuel consumption (TSFC), and the available thrust based on the maximum takeoff thrust of the engine.

In addition to these primary disciplinary analyses, auxiliary modules are included to aid in ensuring that a feasible design is obtained. The first is a stability module that estimates the longitudinal static stability margin of the aircraft based on the method of Torenbeek [52] paired with aerodynamic derivative approximations from DATCOM [59]. The second is a buffet module that helps in limiting the design lift coefficient of the aircraft. This is achieved by performing an analysis on the cruise segments of the long-range, nominal-range, and high-speed cruise missions with a $1.3g$ load factor for maneuverability, and a 0.05 Mach overspeed from the high-speed cruise point. Buffet onset is detected based on the assumed precedence of strong shock formation over the primary lifting surfaces. This is modeled to first order with the wave drag estimation method of Malone and Mason [51], with the assumption that a strong shock will be present when the slope of the drag rise region becomes significantly higher than 0.1. This slope is calibrated based on certified transport aircraft, which are assumed to be buffet-free over their operating envelopes. The metric is then given by the ratio of the free-stream Mach number to the drag divergence Mach number determined at the increased drag rise slope and averaged based on a wing-area weighting over each wing strip.

For optimization, `Faber` uses a gradient-based optimization algorithm to drive the design toward a minimum fuel solution, while maintaining the feasibility of the concept through linear and nonlinear constraints. Gradients are calculated with finite-difference approximations, which are relatively inexpensive in terms of computational cost when used in conjunction with low-order models. Although multimodality may be a concern, solutions with significant differences in their design features and performance are not expected with a properly constrained design space. Details on the design variables and constraints are provided in Section III.A.

As a conceptual design tool, `Faber` provides design weights such as MTOW, the maximum zero fuel weight (MZFW), the operating empty weight (OEW), and the maximum fuel weight (MFW), as well as the weight of the aircraft at all points along a given mission profile for each mission. In addition, `Faber` provides low-order estimates

for the drag of the aircraft components not included in the high-fidelity simulations, and the engine efficiency during cruise. Along with the fuel burned over the off-design conditions, `Faber` enables the calculation of the block fuel burn of a given aircraft, which is the performance metric of interest in this work. `Faber` also plays an important role in providing the information necessary for defining the lift, trim, minimum wing volume, and minimum maximum thickness-to-chord ratio constraints included in the high-fidelity aerodynamic shape optimization studies.

III. Conceptual Design

A. Sizing Problem Formulation

The conceptual designs of the strut-braced-wing and conventional tube-and-wing aircraft are based on a regional jet similar to the Embraer E190-E2, which has a maximum passenger payload of 104 PAX, a design range of 3,100 nmi, and nominal operating conditions at Mach 0.78 and an altitude of 37,000 ft. These aircraft are herein referred to as the SBW100 and CTW100, respectively. Each aircraft is equipped with power plants based on the PW1919G engine [60] with a maximum takeoff thrust of 20,860 lb, a dry weight of 4,800 lb, an engine length and inflow diameter of 187.0 in and 81.0 in, respectively, and a cruise TSFC of 0.587 lb/lb/hr. These parameters are held fixed for the CTW100, since the aircraft is meant to represent the Embraer E190-E2, but can be resized for the SBW100 through the rubber-engine model described in Section II.B.

For the sizing procedure, each aircraft is designed to satisfy the design missions specified by the payload-range diagram shown in Figure 4, which is based on the airport planning manual of the Embraer E190-E2 [61]. These payload-range points are the maximum payload range (R1) point, which is used to size the maximum takeoff weight (MTOW) and most of the fixed weights of each aircraft; the maximum fuel range at MTOW (R2) point, which determines the maximum fuel weight (MFW); and the nominal range (NR) point, which represents a typically-flown mission for regional jets of this type. The objective for each conceptual-level MDO problem is to minimize the block fuel burn over the NR mission, which involves transporting the design payload of 104 PAX over a range of 500 nmi.

Since the CTW100 is intended to represent the Embraer E190-E2 as a performance baseline for comparisons with the SBW100, the aircraft and engines are modeled as-drawn, with all operating conditions specified based on the reference aircraft. This comes with the exception of the thickness distribution of the wing, which is not public knowledge. As such, thickness-to-chord ratio design variables are included at the centerline, root, crank, and tip, and are linearly interpolated across each wing segment. To ensure that there is sufficient fuel capacity to store the maximum usable fuel, these degrees of freedom are bounded by a minimum fuel volume constraint. For wing weight estimation, the wing root is assumed to be clamped, and primary structures are assumed to be constructed from 7075-T6 aerospace grade aluminum alloy, as per Andrews, Perez, and Wowk [53].

For the conceptual design of the SBW100, a number of design variables are included to enable the sizing and

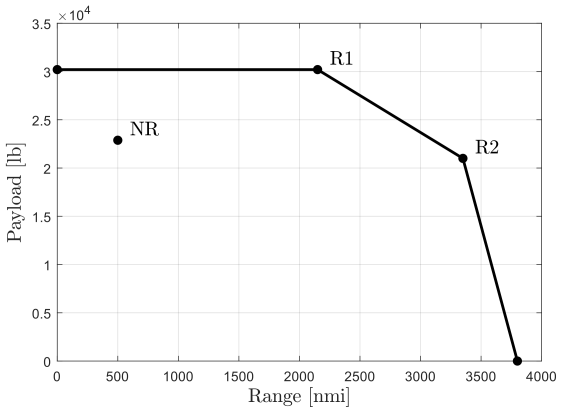

Fig. 4 Payload-range diagram based on the Embraer E190-E2, which includes the maximum payload range (R1) point, the maximum fuel range at MTOW (R2) point, and the nominal range (NR) point.

optimization of the wing and tail systems, the propulsion system, and the initial cruise altitude of each design mission. These degrees of freedom are listed in Table 1. The wing span, wing sweep, and wing-strut junction position are not included as design variables since they are anticipated to be beyond the capabilities of the low-order models, requiring high-fidelity structural and aeroelastic modeling. Instead, these parameters are set or constrained based on strut-braced wings found from the literature which have been subjected to higher fidelity considerations, as will be described below.

Since takeoff and landing are not explicitly modeled in `Faber`, constraints are imposed on the design wing loading and thrust-to-weight ratio to ensure that sufficient wing area and thrust are available under these conditions. In particular, a maximum bound of 110.2 lb/ft^2 is imposed on the wing loading, while the thrust-to-weight ratio is constrained to be greater than or equal to 0.336. These values are chosen based on the reference aircraft, which, despite leading to a more conservative design, avoids the challenge of designing the high-lift systems and predicting low-speed aerodynamic performance, while guaranteeing that the aircraft can operate within a similar envelope. Furthermore, secondary wing weights are calculated assuming that the size and type of the slats, flaps, spoilers, and ailerons are similar to those of the reference aircraft. These assumptions allow for a first-order performance evaluation of the aircraft configuration without the burden of designing new high-lift systems and control surfaces.

With emphasis on the design of an efficient high-speed wing system, the design of the strut-braced wing targets an aspect ratio of around 16-20. This decision is based on the Boeing SUGAR High (765-095-RD-DF), which offers a 30% greater wing span relative to current conventional single-aisle aircraft, which themselves are limited by code C gate restrictions at 118 ft [13]. Since current regional jets have yet to reach the same gate restrictions, it can be difficult to gauge how much of a span increase one can obtain through a strut- or truss-braced wing topology, relative to a cantilever wing that is not gate-limited. Designing the wing system based on a range of aspect ratios can prove to be more concrete, especially when these values are more readily available in the literature and are not as dependent on the class of aircraft considered. For these reasons, the SBW100 is designed with a 136 ft wing span, which, when

Table 1 Design variable information for the conceptual-level MDO of the SBW100.

Design Variable	Quantity	Bounds
Thickness-to-chord ratio, t/c	8	$0.8(t/c)_{\text{init}} \leq t/c \leq 1.5(t/c)_{\text{init}}$
Chord, c	8	$0.5c_{\text{init}} \leq c \leq 2.0c_{\text{init}}$
Horizontal tail chord, c_{h}	2	$0.5c_{\text{init}} \leq c_{\text{v}} \leq 2.0c_{\text{init}}$
Horizontal tail span, b_{h}	1	-5.0 ft $\leq b_{\text{h}} \leq +5.0$ ft
Horizontal tail x-location, x_{h}	1	-10.0 ft $\leq x_{\text{h}} \leq +10.0$ ft
Horizontal tail z-location, z_{h}	1	-10.0 ft $\leq z_{\text{h}} \leq +10.0$ ft
Vertical tail chord, c_{v}	2	$0.5c_{\text{init}} \leq c_{\text{v}} \leq 2.0c_{\text{init}}$
Vertical tail span, b_{v}	1	-5.0 ft $\leq b_{\text{v}} \leq +5.0$ ft
Vertical tail x-location, x_{v}	1	-10.0 ft $\leq x_{\text{v}} \leq +10.0$ ft
Maximum thrust, T	1	18,000 lb $\leq T \leq$ 28,000 lb
Initial cruise altitude, ICA	3	34,000 ft $\leq$ ICA $\leq$ 46,000 ft
Total	**29**	–

combined with the maximum wing loading constraint of 110.2 lb/ft^2, results in a suitable aspect ratio. To accommodate the code C gate restriction at 118 ft, a wing folding mechanism is included at approximately 87% semispan.

In this work, all wing designs assume fully-turbulent flow since natural-laminar-flow technology is not considered. For this reason, the strut-braced wing is designed with a half-chord sweep angle of 30 degrees to maximize wave drag performance at Mach 0.78. This decision, as well as the relative positioning of the wing and strut roots along the fuselage are based on cruise sensitivity studies that can be found in the Boeing SUGAR High technical report [13]. For interference drag, conventional drag factors are adopted for the wing-fuselage, strut-fuselage, and wing-nacelle-pylon junctions. Meanwhile, a T-tail-like interference factor is applied at the wing-strut junction under the assumption that the final design obtained from high-fidelity aerodynamic shape optimization will experience minimal transonic interference effects.

As with Bradley, Droney, and Allen [13], the conceptual design of the SBW100 assumes that the strut does not aid in generating lift. This is a reasonable assumption since high-speed Euler-based [20], and low-speed RANS-based [21] strut-braced wing optimization studies have shown that negative lift on the strut may be required to alleviate interference effects towards the wing-strut junction. As a consequence, however, the optimizer tends to produce a relatively thick strut to withstand buckling, which leads to poor wave drag performance when operating at high transonic Mach numbers. As a pure structural member that generates drag, the optimizer also tends to reduce chord length to achieve reductions in wetted area. To prevent this, a maximum thickness-to-chord ratio constraint of 0.12 is introduced, which forces the optimizer to adopt larger chord lengths to achieve a similar level of flexural rigidity. The problem is further simplified by constraining the strut design to have a constant thickness-to-chord ratio and chord length distribution.

Since `Faber` does not model the sectional shape design of the wing, and it is assumed that both the required C_L and the optimal spanwise lift distribution can be achieved through high-fidelity aerodynamic shape optimization given a reasonable planform design (i.e. there is sufficient wing area, and both taper and aspect ratios are reasonable), linear constraints are introduced to maintain the feasibility of the wing planform. For instance, the optimizer is constrained to maintain a constant chord inboard wing segment, which would otherwise be designed with a taper ratio that exceeds unity. This is because the optimizer tends to design the wing planform according to the out-of-plane bending moment distribution, which decreases towards the midspan of the wing segment before increasing towards the wing-strut junction. This is also because the optimizer favors reductions in viscous drag through smaller chord lengths at the wing root when interference losses at the wing-fuselage junction are not modeled. The optimizer, however, is still permitted to reduce the thickness-to-chord ratio towards the root for a more efficient distribution of structural depth. This results in wing designs that are similar to those that can be found in the literature [11–13].

For structural sizing, the wing structures are constructed from Boeing's advanced quasi-isotropic material [13]. The wing and strut roots are assumed to be clamped, and the wing-strut junction is modeled as a rigid joint, which offers the best structural performance for joined wing systems [62]. The wing-strut junction is positioned at 55% semispan based on the work of Bradley, Droney, and Allen [13]. This represents a reasonable tradeoff between load alleviation from the strut over the inboard portion of the wing, and higher axial loads over the strut when under compression. This decision, however, leans more towards a conservative design without a jury strut to elevate the buckling modes to higher frequencies.

For the SBW100, fuel storage is assumed to be available within both the wing and strut. In addition, a fuel basin is included within the fuselage, which allows for additional fuel capacity up to the equivalent of the fuel storage within the carry-through portion of the CTW100. This limit is set to avoid occupying any space reserved for baggage and internal structures. Both aircraft also include an additional center fuel tank sized based on the Embraer E190-E2.

In order to resize the tail system as the wing design evolves, minimum volume ratio constraints are imposed on the horizontal and vertical tails. These bounds are based on the Boeing SUGAR High, but scaled down from those of a single-aisle aircraft to those of a regional jet, and adjusted to accommodate a higher horizontal tail sweep for improved wave drag performance at Mach 0.78. To maintain a similar level of aerodynamic and structural performance to the reference tail system, linear constraints are also applied to keep the taper and aspect ratios of the horizontal and vertical tails fixed. Finally, linear constraints are imposed on the horizontal and vertical tail locations to maintain the same relative position on the fuselage, as well as the same relative alignment between the horizontal and vertical tails as the planform designs evolve.

For unconventional wing systems like the strut-braced wing, which inherently benefit from lower induced drag at the cost of higher viscous drag at cruise, conventional lift coefficients can lead to suboptimal aerodynamic performance. To address this, the initial cruise altitude of each design mission is allowed to vary, thus permitting the optimizer to

achieve a higher and more optimal cruise C_L to re-balance the parasitic and induced drag components at a fixed wing loading. It should be noted, however, that the objective is to minimize block fuel burn, which places achieving a higher aerodynamic efficiency through higher mission lift coefficients against other competing effects such as increased climb fuel, and increased fuselage weight from the elevated cabin pressurization loads, both of which are modeled in `Faber`. In addition, the buffet heuristic described in Section II.B is used to aid in preventing the sectional lift coefficients from becoming too high, which depends on the airfoil technology factor, thickness-to-chord ratio, and wing sweep.

Finally, the optimizer is constrained to ensure that there is sufficient excess thrust at the start of cruise for a 300 ft/min climb. This forces the optimizer to increase the maximum takeoff thrust of the engines as the aircraft is designed for higher cruise altitudes, which results in an increase in the weight and drag of the propulsion system via the rubber-engine model discussed in Section II.B. With regard to engine placement, the propulsion systems are located at similar relative positions along the wing to the Boeing SUGAR High [13]. For a summary of the nonlinear constraints included in the conceptual-level MDO of the SBW100, see Table 2.

B. Results

Through conceptual-level MDO, optimized designs are obtained for each regional aircraft. The gradient-based optimizations successfully converged feasibility to machine precision, with optimality reducing by 4 to 5 orders of magnitude, and block fuel for the NR missions converging to an asymptotic value. For the optimized CTW100, the minimum fuel volume constraint is active, which is typical for conventional wing designs that are designed for minimum fuel burn or maximum aerodynamic efficiency. On the other hand, the same constraint is inactive for the optimized SBW100. This is due to the lower fuel requirement, as well as the excess fuel storage availability within the strut.

For the SBW100, the design wing loading reaches its maximum bound, effectively sizing the wing area of the aircraft. The minimum thrust-to-weight constraint is inactive at the local optimum. Instead, the propulsion system is sized by the top-of-climb thrust requirement of the MFR mission, which demands more thrust at altitude, thus requiring an increase to the maximum takeoff thrust parameter. The buckling constraints are also active for the optimized design. In particular, the inboard wing segment is found to be limited by the buckling criterion during the $+2.5g$ balanced maneuver, and the main strut is sized against buckling during the $-1g$ dive condition. The buffet margins are not a factor in the optimized design, despite the high cruise lift coefficient. This is likely due to the combination of the large wing sweep, and the thinner wings, leading to better wave drag performance. Finally, both tail volume constraints are found to be active at the local optimum. The state of each group of nonlinear constraints for the optimized SBW100 is listed in Table 3.

The results of the conceptual-level MDO are provided in Table 4. For the CTW100, the design weights of the as-drawn aircraft are in good agreement with the Embraer E190-E2, which has an MTOW of 124,340 lb, an MZFW of 102,514 lb, an OEW of 72,752 lb, and an MFW of 30,203 lb [61]. Compared to this reference aircraft, the optimized

Table 2 Nonlinear constraints for the conceptual-level MDO of the SBW100.

Constraint	Quantity	Bound	Description
Minimum fuel volume	1	–	Constrains the fuel storage capacity based on the maximum usable fuel, MFW
Maximum wing loading	1	110.2 lb/ft^2	Constrains the wing area based on a specified maximum MTOW/S_{ref}
Minimum thrust-to-weight ratio	1	0.336	Constrains the maximum takeoff thrust based on a specified T/MTOW
Minimum top-of-climb thrust	3	–	Constrains the thrust available at start of cruise to have sufficient excess for a 300 ft/min climb for each design mission
Minimum static margin	2	0.05	Constrains the static margin at the start and end of cruise for the NR mission.
Minimum buckling margin	5	–	Ensures that any wing segment under compression does not exceed the critical buckling load with a safety factor of 1.5
Minimum buffet margin	12	–	Constrains the relaxed drag divergence Mach number at four separate Mach-C_L points on the buffet envelope to not exceed the cruise Mach number; this buffet envelope analysis is performed separately for each design mission
Minimum horizontal tail volume ratio	1	1.126	A minimum horizontal tail volume ratio constraint
Minimum vertical tail volume ratio	1	0.054	A minimum vertical tail volume ratio constraint
Total	**27**	–	–

Table 3 SBW100: Nonlinear constraint states at the optimum point of the conceptual-level MDO study.

Constraint	State
Minimum fuel volume	Inactive
Maximum wing loading	Active
Minimum thrust-to-weight-ratio	Inactive
Minimum top-of-climb thrust	Active
Minimum static margin	Inactive
Minimum buckling margin	Active
Minimum buffet margin	Inactive
Minimum horizontal tail volume ratio	Active
Minimum vertical tail volume ratio	Active

SBW100 has the advantage of a 24.6% lower wing weight through a combination of higher structural efficiency offered by the strut-braced wing topology, and the use of lighter weight composite materials. The SBW100 also has an overall lighter tail system primarily owing to a smaller horizontal tail design that is enabled by the larger moment arm of the T-tail configuration. On the other hand, the larger moment arm, along with penalties associated with the high-wing configuration lead to a 11.9% higher fuselage weight, the former of which represents the bending loads experienced by the fuselage in the empirical model. However, based on the weight model given by Torenbeek [52], the fuselage weight is not impacted by the elevated cabin pressurization loads at the design cruise altitudes.

In terms of aerodynamic performance, the high aspect ratio and low thickness wing of the SBW100 provides a 16.0% higher lift-to-drag ratio during nominal-range cruise. This comes in spite of the higher wetted area of the joined wing system. Although combinations of high wing aspect ratio and sweep can lead to nose-up pitching moments if wing stall is encountered at low speeds [63], the 30 degree sweep angle is accompanied by a more modest aspect ratio of 16-17 when compared to the lower sweep and higher aspect ratio of the Boeing SUGAR High, helping the SBW100 to remain less susceptible to this phenomenon. Accounting for increased climb fuel, the SBW100 has an optimal initial cruise altitude of 44,670 ft, which provides a design C_L of 0.68. Overall, the SBW100 benefits from a 9.3% lower block fuel burn over the NR mission, relative to the CTW100, based on the low-order models. Figure 6 depicts the optimized designs modeled in `Faber`, which form the basis for creating the models used in the high-fidelity aerodynamic shape optimizations that follow.

IV. High-Fidelity Aerodynamic Shape Optimization

A. Baseline Geometries

Based on the conceptual designs provided by `Faber`, high-fidelity wing-fuselage-tail models of the CTW100 and SBW100 regional jets are created. For both aircraft, the fuselage nose and tail designs are modeled based on the Airbus A220-300 [64], which is assumed to have a fuselage design that is representative of modern airliners ranging from large regional jets to small single-aisle aircraft. This fuselage design is scaled down to the regional jet class with an equivalent circular diameter consistent with the low-fidelity models used by `Faber`. For the CTW100, the wing-fuselage fairing is also based on the Airbus A220-300, while for the SBW100, the wing-fuselage and strut-fuselage fairings are based on those of the PADRI strut-braced-wing geometry [18].

The baseline wing designs are generally untwisted and defined by RAE-2822 airfoil profiles, which offer suitable transonic performance and provide a good starting point for gradient-based optimization. For the SBW100, however, a +2° wing root twist is introduced to shift most of the upper wing surface away from that of the wing-fuselage fairing. This is done to lessen the coupling between wing root twist deformations and wing-fuselage fairing definition since the optimizer does not have direct control over the latter, as will be described in Section IV.C. Such treatment is not required

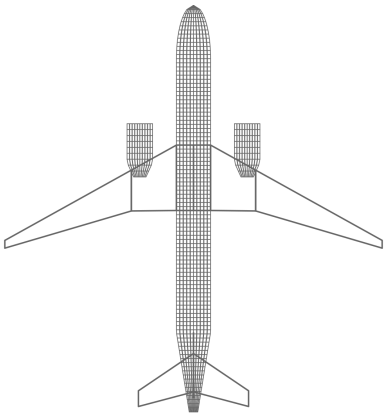

(a) CTW100

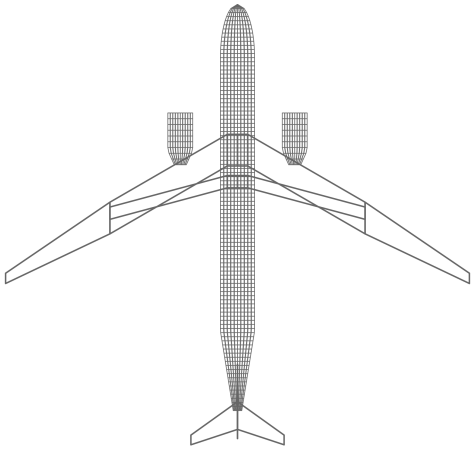

(b) SBW100

Fig. 6 Conceptual designs.

Table 4 Conceptual design results.

Parameter	CTW100	SBW100
Reference MAC [ft]	12.82	8.35
Span [ft]	110.6	136.0
Aspect ratio [–]	10.84	17.32
Wetted aspect ratio [–]	6.39	7.10
Reference area [ft^2]	1,129	1,068
MTOW [lb]	124,290	117,710
MZFW [lb]	102,870	98,790
OEW [lb]	72,670	68,590
Fuselage [lb]	13,480	15,090
Wing [lb]	13,770	10,390
Horizontal tail [lb]	1,320	700
Vertical tail [lb]	710	720
Landing gear [lb]	4,810	4,560
Nacelle and pylon [lb]	3,250	3,170
Propulsion [lb]	12,360	11,750
Systems [lb]	17,540	17,080
Operational items [lb]	3,830	3,830
Unusable fuel [lb]	1,600	1,390
MFW [lb]	30,130	26,200
Maximum takeoff thrust (per engine) [lb]	20,860	19,780
Cruise TSFC [lb/lb/hr]	0.5872	0.5900
Mach number [–]	0.78	0.78
Initial cruise altitude [ft]	37,000	44,670
Reynolds number [$\times 10^6$]	22.04	9.92
Cruise L/D [–]	18.1	21.0
Cruise C_L [–]	0.47	0.68
Cruise C_D [–]	0.0259	0.0324
Cruise drag [lb]	5,620	4,610
Block fuel [lb]	5,160	4,679

[1]All operating conditions and cruise parameters are in reference to the start of cruise for the NR mission

for the CTW100 since the wing intersects with a relatively flat region of the wing-fuselage fairing. The baseline strut design of the SBW100 is untwisted and uses symmetric supercritical SC(2)-0012 sections, since the strut is assumed to be non-lifting. For the horizontal tails of each aircraft, the airfoil sections are defined by SC(2)-0010 profiles that remain fixed throughout the optimization process.

To further aid the optimizer in converging to an optimal design, the thickness distribution across each wing (and strut) is scaled to match the linear distributions provided by `Faber`. In addition, each optimization begins at an angle

of attack that satisfies the C_L target. This ensures that the optimization starts at a design point that is close to the boundaries of the constant lift, minimum volume, and minimum $(t/c)_{\max}$ constraints described in Section IV.D, which we assume will be active for the optimum design.

B. Computational Grids

The computational domain around each aircraft is discretized by a structured multi-block grid with an O-O blocking topology. For optimization, each grid is created based on the *medium mesh* of the Fifth Drag Prediction Workshop (DPW) gridding guidelines [65], which is representative of current engineering drag prediction standards. For the CTW100, the grid consists of 14.41 million nodes partitioned across 558 blocks, while for the SBW100, 26.51 million nodes are partitioned across 1,355 blocks. The difference in the number of blocks, and therefore the number of nodes for a similar number of nodes per block, is a consequence of how the number of blocks scales with geometric complexity for meshes that are structured. Each grid remains consistent in terms of resolution and thus numerical error, however, since each computational domain has a similar grid resolution per unit chord, span, and off-wall distance.

Another difference between the two meshes is that the O-grid blocks surrounding the strut of the SBW100 are nested within a second layer of O-grid blocks that project onto the lower surface of the wing and onto the belly fairing. This results in a buffer zone of surface patches that can be used with the junction deformation scheme described in Section IV.C, without introducing bidirectional boundary-layer mesh nodes, which would otherwise increase convergence time.

In order to obtain an estimate of the grid-converged aerodynamic functionals for the optimized geometries, Richardson extrapolation is performed with two additional grid levels, L1 and L2, which have two and four times as many grid nodes as the optimization grid, L0, respectively. These are generated with the automatic grid refinement capabilities of `Jetstream`, which takes advantage of grid node insertion and redistribution to maintain the original mesh spacing functions while preserving the analytical surface definition [49]. Table 5 provides a summary of the grid families for both the CTW100 and SBW100 aircraft configurations, while the surface meshes and patch topologies of each aircraft are illustrated in Figure 7.

C. Junction Deformation Scheme

In order to provide a means for modifying the wing-strut junction, a patch-based deformation scheme has been developed that is compatible with structured multiblock flow solvers and mesh deformation algorithms. For this method, a buffer zone of *follower* patches on the lower surface of the wing and around the vertical strut is left unembedded from the FFD volumes. Rather than controlling these follower patches directly, they are instead driven by deformations from adjacent *leader* patches, where changes to the control point coordinates of the leader patches are propagated across the mesh lines of the follower patch from each boundary via a linear blending function.

Table 5 Grid information.

Grid	Number of Nodes	Average Off-wall Spacing[1]	Average y^+
	Conventional Tube-and-Wing		
L0	14.41×10^6	8.84×10^{-7}	0.53
L1	27.56×10^6	6.92×10^{-7}	0.41
L2	54.85×10^6	5.36×10^{-7}	0.31
	Strut-Braced Wing		
L0	26.51×10^6	1.91×10^{-6}	0.57
L1	50.50×10^6	1.50×10^{-6}	0.43
L2	99.54×10^6	1.16×10^{-6}	0.33

[1]Off-wall spacings are in units of mean aerodynamic chord

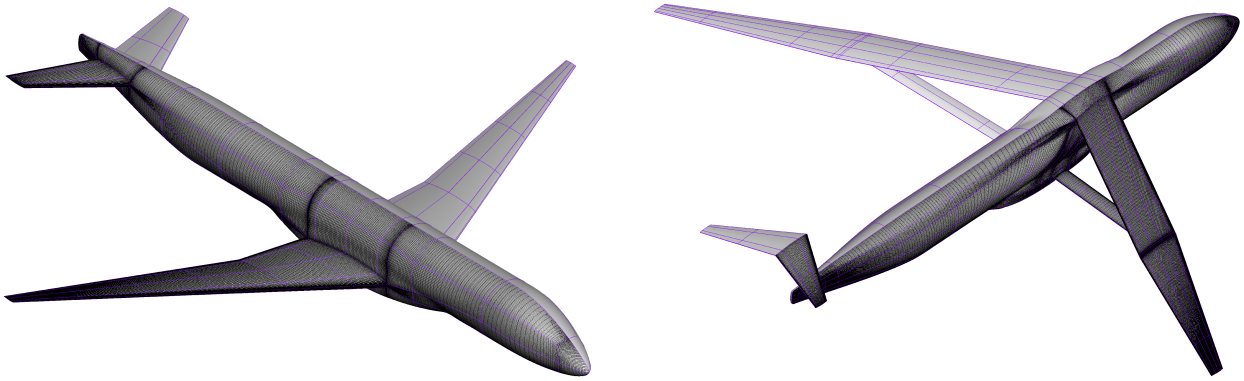

(a) CTW100 **(b) SBW100**

Fig. 7 Surface meshes (L0) and patch topologies.

To ensure that the uppermost edges of the leader patches on the vertical strut remain in line with the leader patches on the wing, the uppermost axial control point and FFD-volume cross-section controlling the vertical strut are embedded within the FFD volume of the wing. Additional FFD-volume cross-sections are introduced nearby and are also embedded within the wing FFD volume. In this way, the uppermost edges of the vertical strut deform with the twist and section shape design variables of the wing, while also being modified by their own FFD-volume cross-sections. To prevent control point crossover when large deformations are applied to the wing, a linear interpolation in the z-direction of the FFD-volume control points is also introduced between the last embedded FFD-volume cross-section and the lowermost FFD-volume cross-section of the vertical strut.

For gradient-based optimization, the linear blending function is captured by aggregating the sensitivities of the objective function to each surface control point across each mesh line of a given follower patch and transferring them to the boundary control points of the adjacent leader patches. Depending on the blocking topology, there can arise

cases where the corner of a follower patch is bordered by three adjacent leader patches. In these instances, the control point sensitivities are shared uniformly across each leader patch control point, thus ensuring that the corner patch also has an influence over the follower patch of interest. For the remaining changes, the sensitivities are integrated into the gradients of the FFD-volume control point coordinates with respect to each design variable, which are computed through the complex step method. This includes the nested axial control point and FFD-volume cross-sections, as well as the FFD-volume control point interpolations.

In order to maintain continuity at the junctions of the wing and fuselage, the strut and fuselage, and the horizontal tail and fuselage, a similar deformation scheme is used, which was presented in the work of Osusky et al. [49]. In this method, each follower patch on a given fairing is only driven by a single leader patch on the wing or strut. Deformations are identical at the boundary between the leader and follower patches, and tend to zero along a given mesh line away from the boundary based on a cosine function, thus preserving a high degree of continuity at the interface. As with the junction deformation scheme described above, control point sensitivities over the follower patches are aggregated and transferred to the boundary control points of the respective leader patch.

To verify that the changes to the sensitivities of the geometry control system and surface parameterizations have been properly accounted for, a directional derivative test is performed using the minimum volume constraint as a test function. In this test, the volume function gradients, which are dependent on the changes described above, are calculated through a contraction of the analytical and complex step derivatives and are compared to finite-difference approximations. Figure 8a shows the results for the CTW100 gradient test, which includes the wing-fuselage junction deformation scheme, while Figure 8b for the SBW100 includes the wing-strut, wing-fuselage, and strut-fuselage junction deformation schemes. Here, it can be seen that at the optimum step size, the difference is less than 10^{-10} for both cases. Figure 9 shows the patch-based deformation scheme setup for each of the junctions of the strut-braced-wing configuration.

D. Optimization Problem Formulation

For detailed aerodynamic design, the CTW100 and SBW100 regional jets are optimized for minimum cruise drag at constant lift and zero pitching moment at the start of cruise for the NR mission. By assuming that all other parameters in the Breguet range equation remain fixed, this is to first order equivalent to minimizing fuel burn at cruise, and by extension, minimum block fuel burn, assuming that all other fuel contributions also remain constant. The optimizer is allowed to vary the angle of attack, as well as a number of geometric design variables that provide control over the wing and horizontal tail surfaces.

The geometric degrees of freedom are realized through the free-form and axial deformation geometry control systems shown in Figure 10. For both aircraft, the wing and horizontal tail surfaces are each embedded within an FFD volume, but for the SBW100, three additional FFD volumes are included to individually control the main strut,

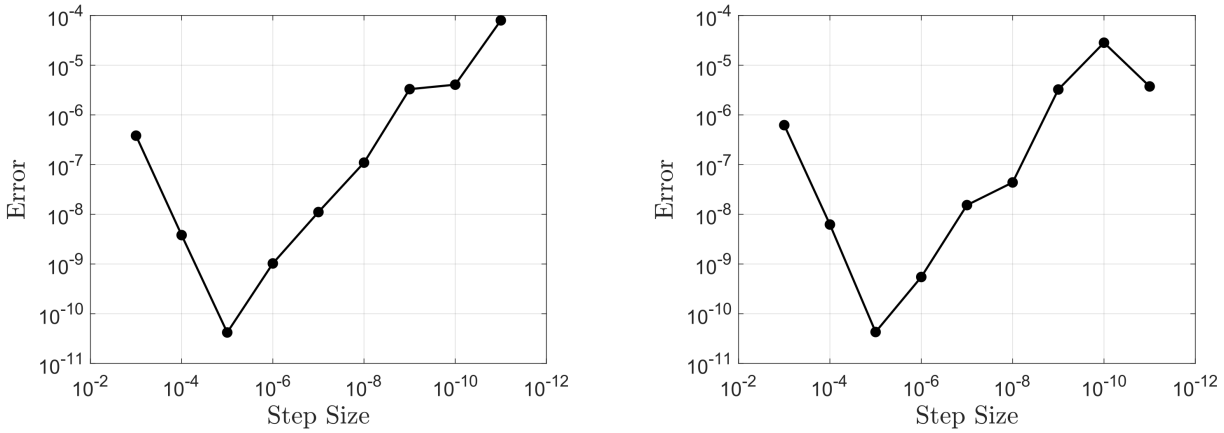

(a) CTW100 **(b) SBW100**

Fig. 8 Directional derivative tests verifying the implementation of the junction deformation schemes. Volume constraint gradients are compared to finite-difference approximations.

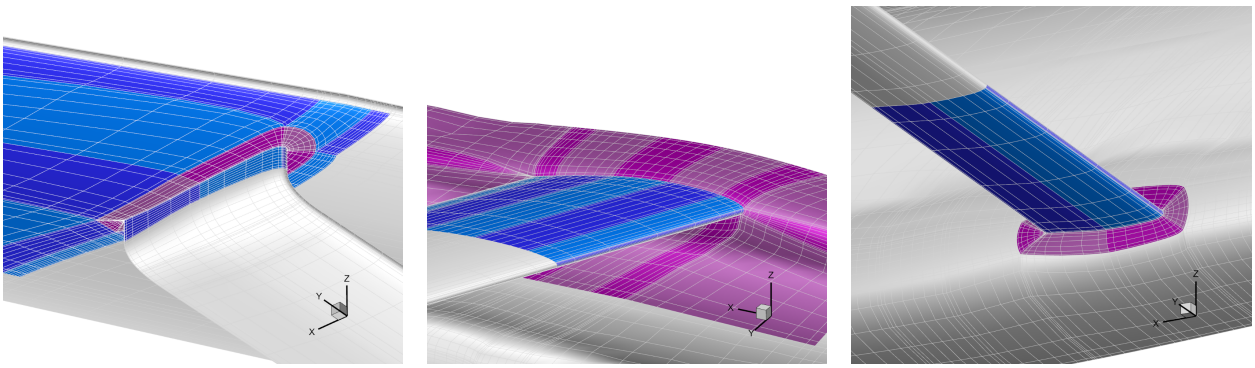

(a) Wing-strut junction **(b) Wing-fuselage junction** **(c) Strut-fuselage junction**

Fig. 9 Patch-based junction deformation setup for the strut-braced-wing configuration, which includes leader patches (blue), follower patches (purple), and surface control grids (white lines).

the vertical strut, and the blended transition. These FFD volumes are defined by a similar number of FFD-volume cross-sections per unit span that each consist of 22 FFD-volume control points divided evenly above and below the aerodynamic surfaces. An exception is made for the SBW100, however, where additional FFD-volume cross-sections are included towards the wing-strut junction to provide additional control where adverse aerodynamic effects are most expected. Smooth variations over the control volumes are provided through cubic interpolations in the chordwise and spanwise directions, and linear interpolations in the vertical direction. Attached to the quarter-chord of each FFD volume is an axial curve, which defines the origin of the local coordinate systems and the points of rotation for the twist design variables.

For the CTW100, the wing design variables include 12 twist and 264 section shape degrees of freedom, while for the SBW100, 38 twist and 836 section shape design variables are included across the wing and strut. For both aircraft, linear constraints are introduced to fix the leading- and trailing-edge positions with respect to the section shape degrees

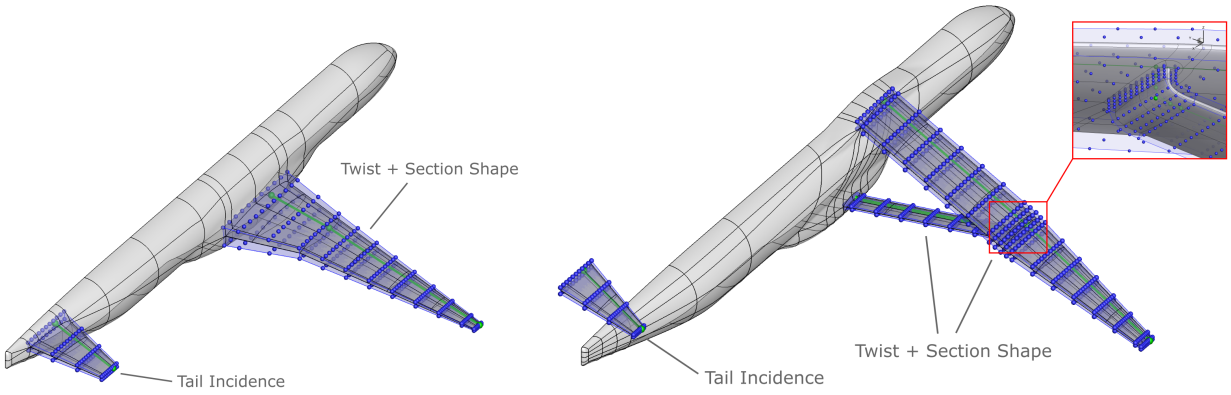

(a) CTW100 **(b) SBW100**

Fig. 10 Geometry control systems with FFD volume entities in blue, and axial curve entities in green.

of freedom. This is accomplished by constraining the section shape design variables above and below the aerodynamic surfaces to have equal and opposite values at each end of a given FFD-volume cross-section. In this way, shear twist is removed from the design space, which is often redundant with the rotation twist degrees of freedom. In addition, this prevents the optimizer from introducing a constant shift up or down to all of the FFD-volume control points, which would cause the wing and strut roots to move.

For the SBW100, linear constraints are introduced to link the twist design variables across the FFD-volume cross-sections of the vertical strut and to impose an interpolation across the transition segment. This is done to prevent the optimizer from designing a strut with large curvature and excessive waviness, which was uncovered during earlier design iterations where the optimizer exploited the nonlinear twist degrees of freedom to alleviate shock formation, boundary-layer separation, and interference effects within the wing-strut junction. Although novel, these features raised major concerns over manufacturability and structural feasibility, and proved to provide only a modest improvement in aerodynamic efficiency. For similar reasons, a linear constraint is imposed to interpolate the twist design variable between the 9th and 11th FFD-volume cross-sections over the wing of the SBW100, which would otherwise often feature a sharp wash-in to compensate for the local loss of sectional lift due to the presence of the strut.

Planform design variables such as taper, sweep, span, and dihedral are excluded to preserve characteristics of the aircraft that have a strong dependence on disciplines other than aerodynamics and that largely influence off-design performance. For similar reasons, minimum maximum thickness-to-chord ratio constraints are introduced at 10 and 30 spanwise locations along the wing of the CTW100, and the wing and strut of the SBW100, respectively. These nonlinear constraints allow for modifications to the magnitude and location of the maximum thickness of a given section while maintaining a lower bound on structural performance based on the stiffness distributions of `Faber`. Although the optimizer can, in principle, exploit the regions between each spanwise location, such an avenue is made more difficult by the cubic interpolations of the FFD volumes in the spanwise direction. Furthermore, linear thickness constraints are

introduced to place a lower bound on the local vertical separation between each chordwise pair of FFD-volume control points. This ensures that the airfoil profile cannot be scaled below 50% of its initial thickness at any given chordwise location and prevents any crossovers of the FFD-volume control points.

For the minimum $(t/c)_{\max}$ constraints, 21 chordwise locations between 0.10 and 0.90 chord are identified on the upper and lower surfaces of the wing and or strut. This is achieved by solving a nonlinear least-squares problem for each point where the objective is to find the parameter w along a vertical line drawn in the parametric space of a given FFD volume that leads to a match in physical coordinates to the (u, v) parameters on a given surface patch. Computing the local chord length in a similar fashion, the thickness-to-chord ratio at a given chordwise and spanwise location can be determined. The number of constraints is then reduced by aggregating the 21 chordwise thickness-to-chord ratio values at a given spanwise location through a Kreisselmeier-Steinhauser formulation [66] that provides a smooth maximum.

In order to ensure that there is sufficient fuel tank capacity for storing the maximum usable fuel, a minimum volume constraint is introduced to place a lower bound on the volume of the wing (and strut) OML. These bounds are determined by the wing (and strut) OMLs of the low-fidelity aircraft models used in `Faber`, which considers the available volume between the fore and aft spars with utilization factor and trapped fuel accounted for. In addition to fuel considerations, this constraint aids in preventing the optimizer from exploiting the spanwise sections between each minimum $(t/c)_{\max}$ constraint, thus playing a part in maintaining a minimum structural depth.

For the horizontal tails, the FFD volumes consist of 4 FFD-volume cross-sections. In both cases, however, the optimizer is allowed to modify only the incidence angle to maintain a symmetric horizontal tail design. This is done by removing section shape degrees of freedom and introducing a linear constraint that links the twist design variables across the FFD volume.

Based on deck angle requirements, the angle of attack is limited to $\pm 3^\circ$, while the twist design variables can vary between $\pm 10^\circ$. Exceptions are made for the twist design variables at the wing root and over the vertical strut of the SBW100, which are limited to $\pm 3.5^\circ$. This is done to ensure that the high-wing fairing maintains its overall shape, and to prevent the strut from twisting beyond the buffer zone of follower patches used by the junction deformation scheme. For the section shape design variables, changes are limited to scaling factors of between 0.50 and 2.0. A summary of the design variables and their bounds is provided in Table 6, while a list of the linear and nonlinear constraints is included in Table 7.

E. Results

For each optimization problem, a given design is considered optimal when the drag coefficient at the start of cruise no longer improves by more than a drag count over 10 or more function evaluations, and when feasibility has been satisfied. Based on this criterion, an optimal design for the CTW100 was obtained following 122 major iterations (or

Table 6 Design variable information for high-fidelity aerodynamic shape optimization.

Design Variable	Quantity		Lower Bound	Upper Bound
	CTW100	SBW100		
Angle of attack	1	1	−3.0 deg	+3.0 deg
Twist	16	42	−10.0 deg	+10.0 deg
Section shape	264	836	0.5	2.0
Total	**281**	**879**	–	–

[1]SBW100 wing root and vertical strut twist bounds are limited to ±3.5 deg.

Table 7 Linear and nonlinear constraint information for high-fidelity aerodynamic shape optimization.

Constraint	Quantity		Description
	CTW100	SBW100	
Lift	1	1	Constrains the aircraft lift to equal the weight at the start of cruise (nonlinear)
Trim	1	1	Constrains the aircraft pitching moment to equal zero (nonlinear)
Minimum volume	1	1	Constrains the minimum wing (and strut) OML volume based on fuel storage requirements (nonlinear)
Minimum $(t/c)_{\max}$	10	30	Minimum maximum thickness-to-chord ratio constraints based on structural requirements (nonlinear)
Minimum t/c scaling	132	418	Constrains the local vertical separation between each pair of FFD-volume control points to be greater or equal to 50% of its initial value (linear)
Fixed LE/TE	24	76	Constrains section shape design variables at the leading- and trailing-edges to be equal and opposite between the lower and upper FFD-volume control points (linear)
Linked horizontal tail twist	1	1	Links the twist design variables of the horizontal tail to translate to incidence angle control (linear)
Linked vertical strut twist	0	1	Links the twist design variables of the vertical strut segment (linear)
Linear transition strut twist	0	1	Interpolates the twist design variables across the transition strut segment (linear)
Total	**170**	**530**	–

133 function evaluations), while for the SBW100, convergence was achieved after 100 major iterations (or 135 function evaluations). In both cases, optimality reduced by approximately an order of magnitude, while feasibility converged to a tolerance of 10^{-5} or better. Although a deeper convergence of these metrics is often preferred, the problem is

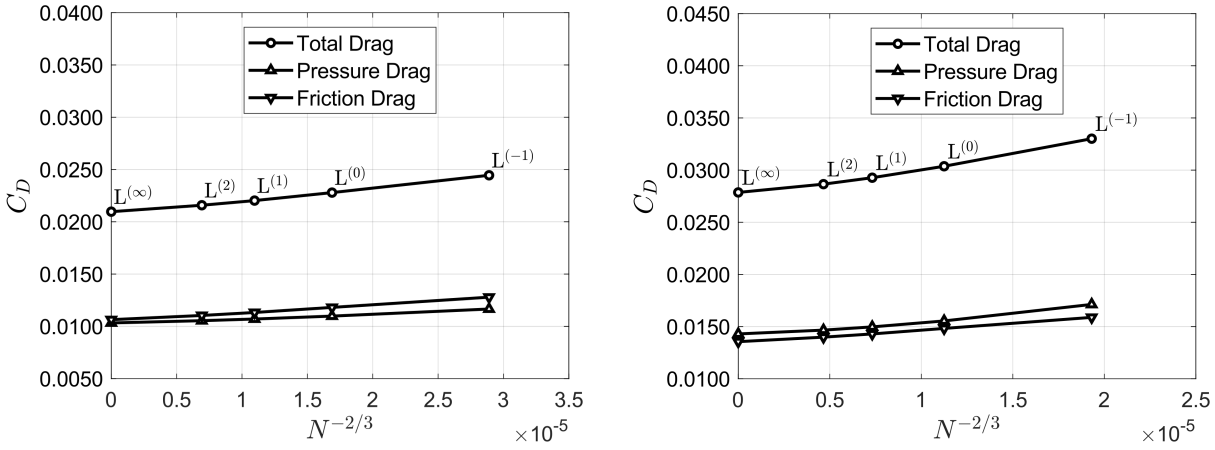

(a) CTW100 **(b) SBW100**

Fig. 11 A grid convergence study of each optimized aircraft at constant lift.

considered sufficiently converged given that the objective function has reached an asymptotic value, and all nonlinear constraints have been satisfied beyond engineering precision.

From the optimized geometries, grid-converged aerodynamic functionals are obtained through Richardson extrapolation, as shown in Figure 11. Here, we refine at constant lift by readjusting the angle of attack at each grid level. For the CTW100, the mesh-independent drag coefficient is 210 counts, with a 49:51 ratio between pressure and friction drag. Meanwhile, the optimized SBW100 has a drag coefficient of 279 counts, and a 51:49 pressure-to-friction drag ratio. These translate to lift-to-drag ratios of 22.3 and 24.5 for the optimized CTW100 and SBW100 regional jet aircraft, respectively, or a 9.5% improvement in cruise L/D and a 12.9% reduction in cruise drag for the SBW100 over the CTW100.

Applying a 5% markup on the skin friction drag component to account for excrescence drag, and combining these results with the low-fidelity estimates for drag contributions from the vertical tail, nacelles, and pylons, the improvement in aircraft cruise L/D becomes 12.9% for the nominal range mission. Similarly, the reduction in cruise drag offered by the optimized SBW100 becomes 15.5%, when compared to the optimized CTW100. Accounting for the quantity of fuel required for warmup, taxi, takeoff, climb, descent, and landing, the block fuel for each aircraft is found to be 5,028 lb and 4,643 lb, respectively. This provides a 7.6% reduction in block fuel for the SBW100, when compared to the equivalently optimized and designed CTW100. These results are summarized in Table 8.

For both optimizations, the minimum volume constraints are active at the optimum point. Meanwhile, the minimum maximum thickness-to-chord ratio constraints are more of a limiting factor for the CTW100 than the SBW100. For the CTW100, much of the wing volume is distributed towards the inboard portion of the wing, as shown in Figure 12a, which is typical for aerodynamic shape optimization problems where the minimum volume constraint is a limiting factor, and when structural analyses are not included. This results in improved wave drag performance over the outboard

Table 8 Optimized aircraft performance.

Parameter	CTW100	SBW100	Δ
	High Fidelity[1]		
L/D [–]	22.3	24.5	+9.5%
C_L [–]	0.47	0.68	+45.6%
C_D [–]	0.0210	0.0279	+32.9%
Lift [lb]	101,720	97,000	−4.6%
Drag [lb]	4,555	3,966	−12.9%
	Low and High Fidelity[2]		
Cruise L/D [–]	19.0	21.4	+12.9%
Cruise C_L [–]	0.46	0.68	+45.6%
Cruise C_D [–]	0.0247	0.0318	+28.9%
Cruise drag [lb]	5,365	4,532	−15.5%
Block fuel [lb]	5,028	4,643	−7.6%

[1]Includes only the wing (and strut), fuselage, and horizontal tail contributions.
[2]Includes a 5% excrescence drag markup, and profile drag contributions from the vertical tail, nacelles, and pylons.

portion of the wing, where the sectional lift coefficients can often be larger because of the smaller chord lengths.

For the optimized SBW100, the minimum maximum thickness-to-chord ratio constraints determined by `Faber` are largely inactive across the wing, with the optimized distribution shown in Figure 12b featuring a concave-down form that resembles those from the work of Bradley, Droney, and Allen [13]. This result suggests that such a distribution is optimal beyond structural considerations. For the main strut, the optimized thickness-to-chord ratio distribution is constant at a value of 0.12, with slight deviations, and remains constant over the transition and vertical strut segments.

Here, it should be noted that although the minimum $(t/c)_{\max}$ constraints may impede aerodynamic performance, they are not as punitive when it comes to structural weight. This is because `Faber` is still allowed to vary the structural thicknesses of the booms and skins within the wing and strut OMLs to achieve nonlinear stiffness distributions that closely follow the shear forces and bending moments.

For both optimized aircraft, the angle of attack has been pushed to its upper bound at +3°. The optimized twist distributions are shown in Figure 13. In both cases, the twist design variables remain within their bounds, except at the wing root of the optimized SBW100, which has been limited to +3.5° to prevent excessive changes to the high-wing fairing. Although not shown in Figure 13b, the strut twist at the end of the main strut is linearly interpolated across the transition strut from −2.591° to −2.594°, and remains constant over the vertical strut as a consequence of the linked vertical strut twist constraint.

Figure 14 shows the spanwise lift distributions of the optimized CTW100 and SBW100 aircraft. For the CTW100,

it can be seen that the spanwise lift distribution is elliptical in form over the outboard portion of the wing, but increases significantly towards the root. This can be explained by the trim constraint, which makes it preferable for the optimizer to load the inboard portion of the wing where the nose-down pitching moment contribution is lessened. In addition, the increased wing loading required to counteract the negative lift on the horizontal tail can, in some instances, lead to higher sectional lift coefficients at a fixed chord if an elliptical lift distribution is maintained. In these instances, the optimizer opts to mitigate wave drag penalties by shifting the additional load inboard, at a small cost to induced drag performance. Indeed, a perturbation analysis done by Hicken and Zingg [67] suggests that even moderate deviations from an elliptical lift distribution lead only to small penalties in induced drag.

Similar trends can be seen for the optimized SBW100, but with much greater deviations from the elliptical lift distribution over the outboard portion of the wing. This can be explained by the same mechanisms as for the CTW100, and also by noting that the high-aspect ratio wing extends much farther aft at a similar wing sweep angle, leading to elevated nose-down pitching moments. In addition, the high design C_L of the SBW100, paired with the smaller chord lengths towards the wing tip further exacerbates the tradeoff between mitigating wave drag at the cost of higher induced drag.

As observed by Gagnon and Zingg [20] and Secco and Martins [21], the optimized strut produces negative lift from the quarter-semispan with increasing magnitude towards the wing-strut junction. Such a design feature is one means for relieving the adverse pressure gradients within the junction, which would otherwise lead to shock formation. In order to compensate for this local loss of lift, the optimizer introduces a local increase in sectional lift on the wing, which brings the total lift distribution in that region closer to elliptical. Once again, this phenomenon was observed in the work of both Gagnon and Zingg, and Secco and Martins. Of interest, however, is the positive lift on the strut near the strut root, which was not observed in the previous studies involving high-fidelity aerodynamic optimization. This may be because the optimizer has opted to avoid increasing the inboard wing loading further to prevent wave drag penalties.

Figures 15 and 16 show the overall performance characteristics of the optimized CTW100 and SBW100 regional aircraft, respectively. For the CTW100, Figure 15b illustrates the shock surfaces over the initial and optimized geometries, which have been extracted via the Lovely-Haimes detection method [68]. Here, it can be seen that the shock surfaces present across the upper surface of the initial wing design have been largely eliminated, consistent with the surface pressure distributions shown in Figures 15a and 15c. These shocks can also be seen in the initial pressure distributions included in Figure 15c, which manifest as steep pressure drops over the upper surface contours, with one near the leading edge, and another at approximately 75% chord from 15% semispan to 60% semispan.

Once optimized, the airfoil profiles exhibit smooth pressure recoveries towards the trailing edge and are characterized by wash-out from the wing root out to the wing tip, consistent with the twist distribution shown in Figure 13a. The optimizer has also introduced a narrow leading edge design across the wing that has been seen to be aerodynamically

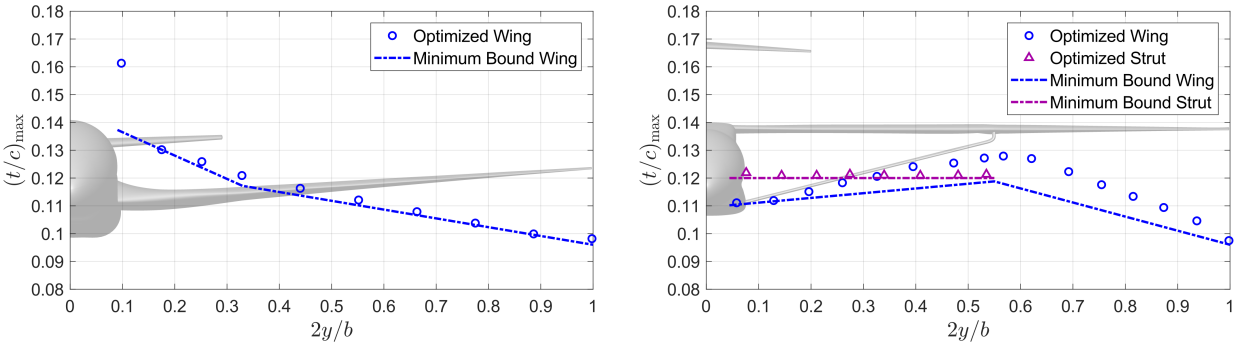

(a) CTW100 **(b) SBW100**

Fig. 12 Optimized maximum thickness-to-chord ratio distributions.

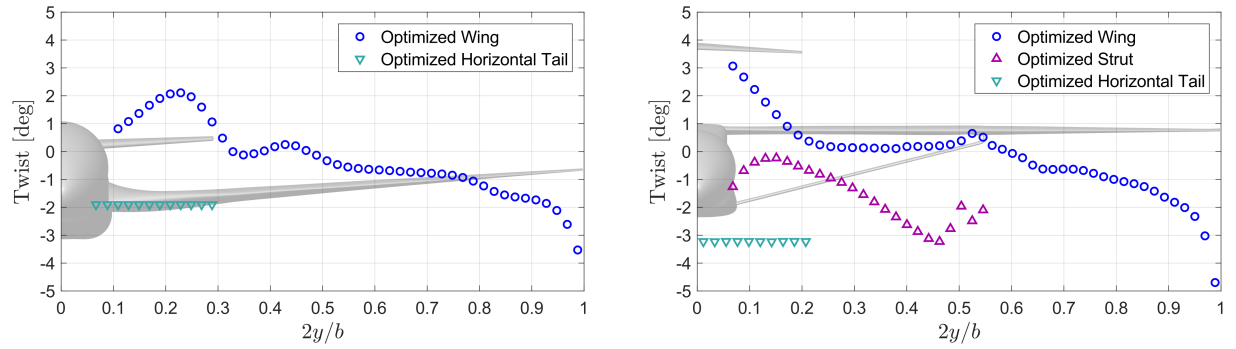

(a) CTW100 **(b) SBW100**

Fig. 13 Optimized geometric twist distributions.

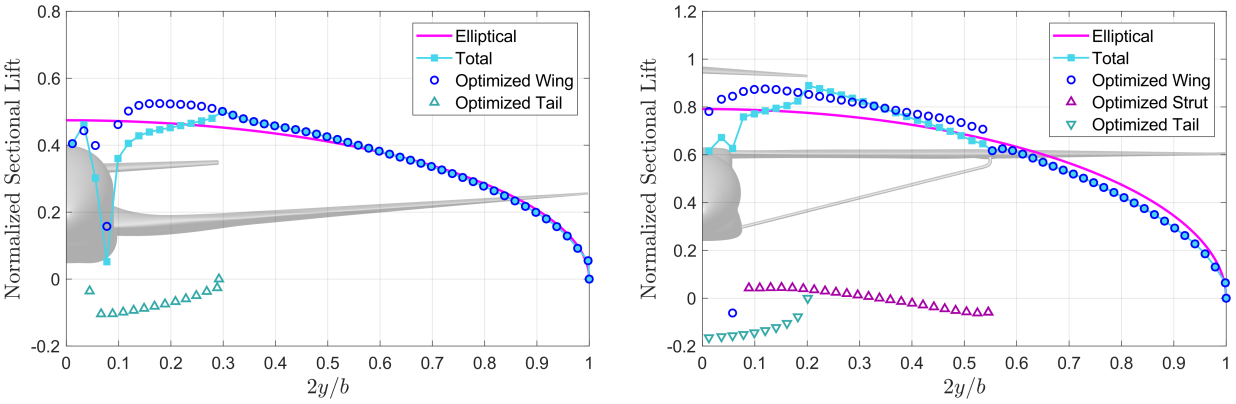

(a) CTW100 **(b) SBW100**

Fig. 14 Optimized spanwise lift distributions.

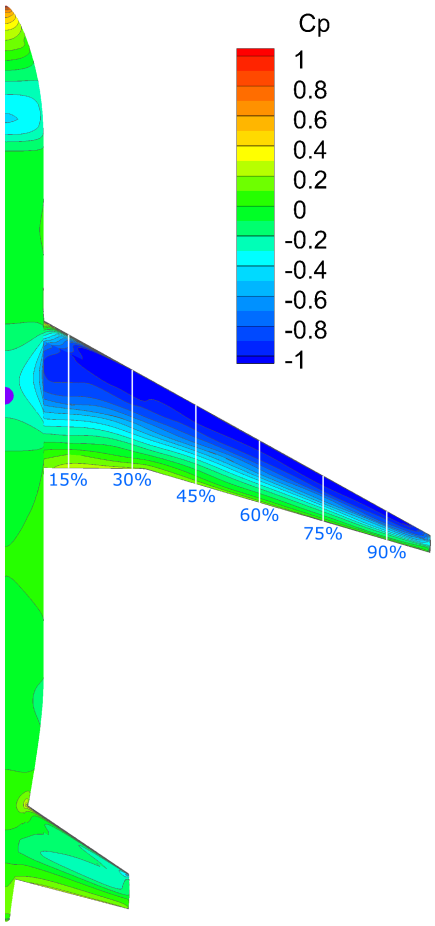

(a) **Optimized surface pressure contours and CG (purple circle)**

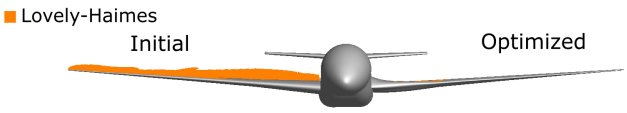

(b) **Shock surfaces**

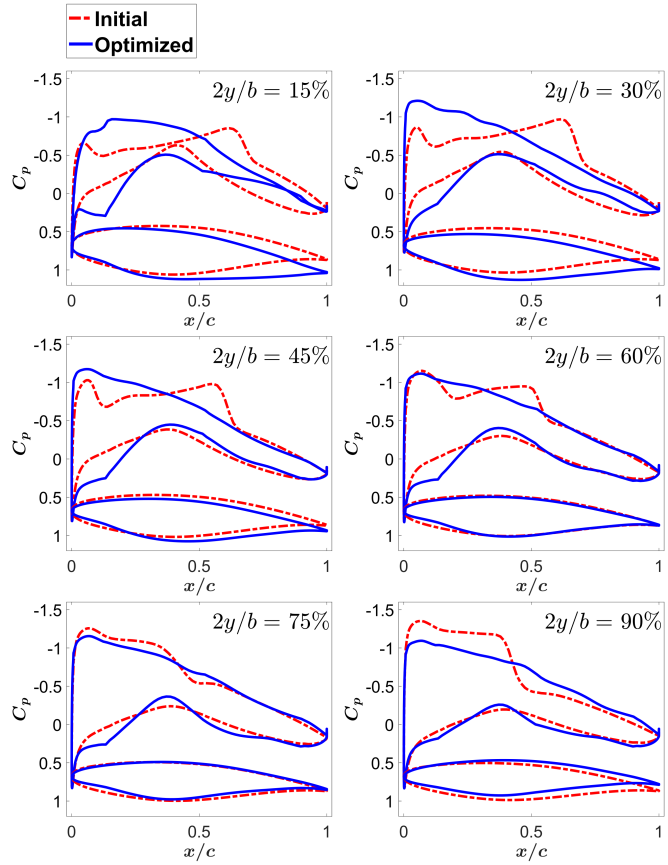

(c) **Pressure distributions**

Fig. 15 CTW100: Optimization results: $\alpha = 3°$, $C_L = 0.47$, $C_D = 0.0210$, $L/D = 22.3$.

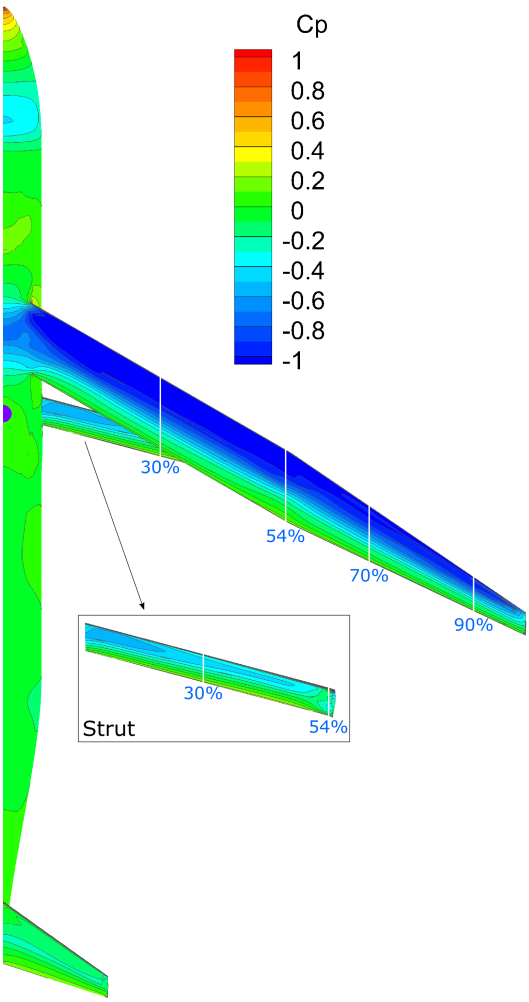

(a) **Optimized surface pressure contours and CG (purple circle)**

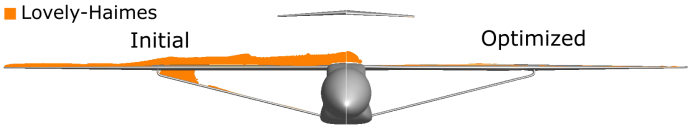

(b) **Shock surfaces**

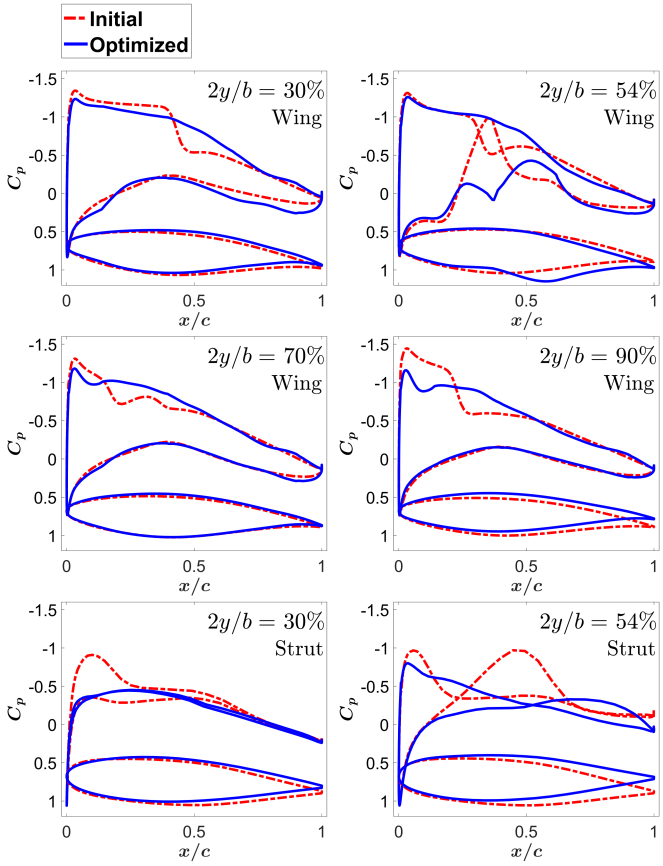

(c) **Pressure distributions**

Fig. 16 SBW100: Optimization results: $\alpha = 3°$, $C_L = 0.68$, $C_D = 0.0279$, $L/D = 24.5$.

favorable in both single- and multi-point optimization problems (see for example, Nemec et al. [69]). Since this can be undesirable from the perspectives of structural design and high-lift aerodynamic performance, minimum leading-edge radius constraints can provide a means for removing them from the design space. This feature is not a concern for the present study, however, given the consistency maintained between the two aerodynamic shape optimization problems, and since it is not expected to overly impact the overall performance of these representative aircraft designs.

As shown in Figure 16b, the shock surfaces present across the initial wing geometry of the SBW100 have also been largely mitigated through optimization. Although shock surfaces may remain near the leading edge, as illustrated by the pointed suction peaks in Figure 16c, the upstream Mach numbers perpendicular to the shocks are 1.1 or less, indicating that any shocks are weak and introduce little wave drag. The optimized SBW100 is also shock-free within the wing-strut junction. As illustrated by the airfoil profiles at 54% semispan shown in Figure 16c, the strut section features a flattened upper surface that produces a modest quantity of lift, before the camber is inverted, providing negative lift towards the trailing edge, presumably to provide a more favorable pressure gradient aft of where the shock is located on the initial geometry. Indeed, as demonstrated by Ko, Mason, and Grossman [17], flattening the upper surface of the main strut aids in alleviating the transonic nozzle effect, and contributes to preventing shock formation. At the same time, the lower surface of the wing section features a large bulge, which appears to decrease the local pressure to reduce the difference with the upper surface of the strut.

Figure 17 allows for a closer inspection of the flow phenomena surrounding the wing-strut junction. Here, surface pressure contours are shown for the initial and optimized geometries, with views of the inside and outside surfaces of the strut. For clarity, the initial and optimized geometries have not been rotated about the y-axis with respect to the angles of attack. Streamwise slices have been extracted normal to the axial curve and along the parametric spanwise direction for both the wing and strut. As can be seen in Figure 17b, the transonic channel effect causes the pressure distribution to rapidly increase over the lower and inner surfaces of the initial wing and strut geometries, respectively, before the formation of a shock leads to a large adverse pressure gradient. This occurs even though the airfoil profiles of the strut are initially symmetric with no geometric twist, albeit at a non-zero angle of attack. Once optimized, the steady rise and fall of the inner surface pressure distribution is reduced, resulting in a modest sectional force distribution that is directed outwards. Overall, this leads to a spanwise lift distribution that has been shown to be optimal based on linear aerodynamic theory [70].

The positive impact of these design features are even more evident in Figure 18, where streamlines are plotted over the bottom surface of the wing and the inner surface of the strut for the initial and optimized SBW100 geometries. It can be seen that the presence of the shock within the wing-strut junction of the initial geometry has resulted in two distinct flow separation regions. For the optimized design, these adverse effects have been eliminated.

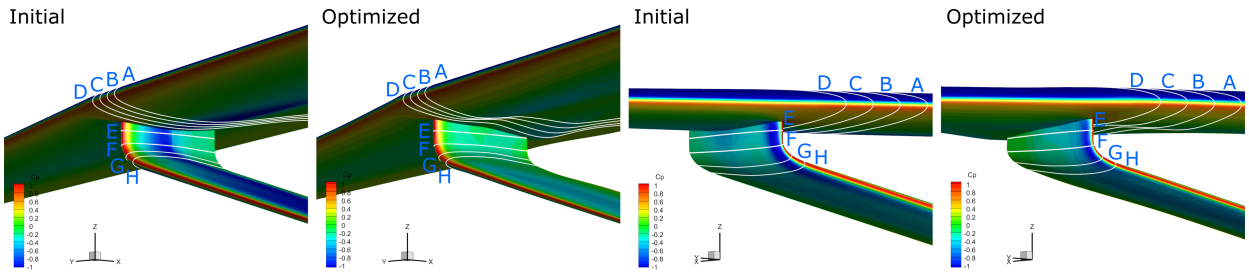

(a) Surface pressure contours

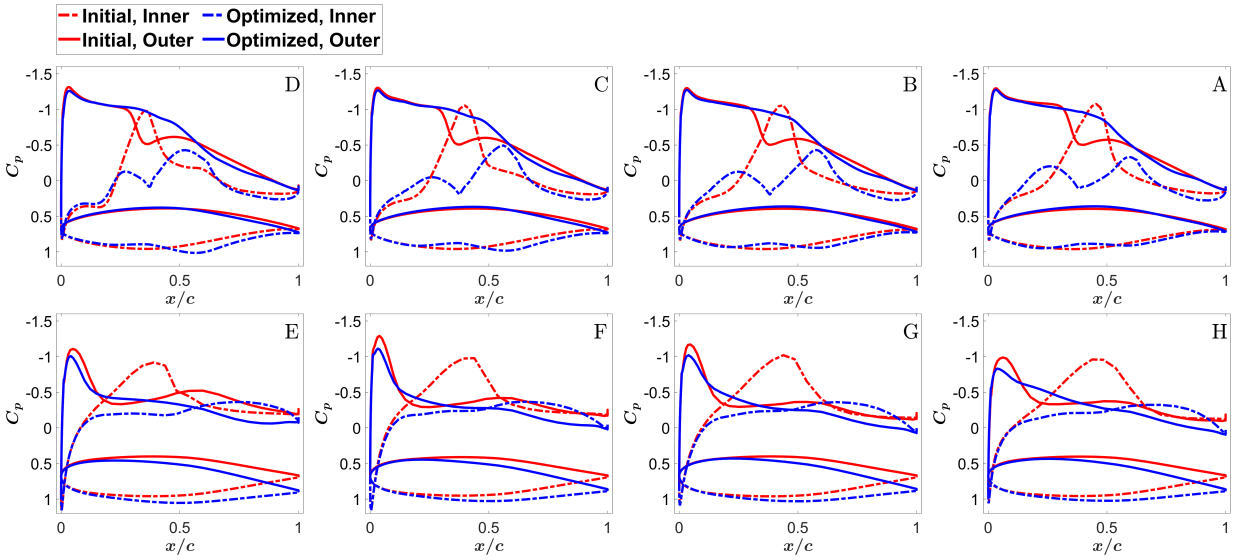

(b) Pressure distributions

Fig. 17 SBW100: Surface pressure contours with inner [(a), left] and outer [(a), right] views of the strut, and pressure distributions at different stations along the wing and strut.

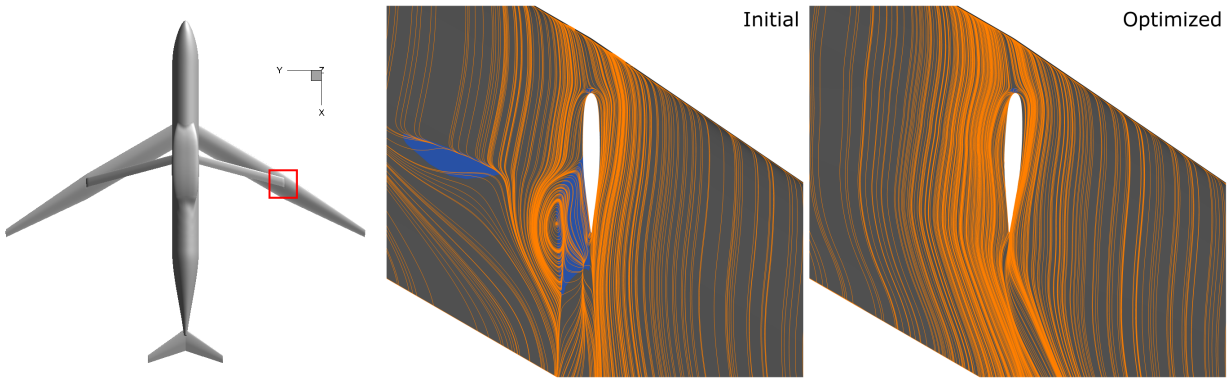

(a) Lower surface of the wing

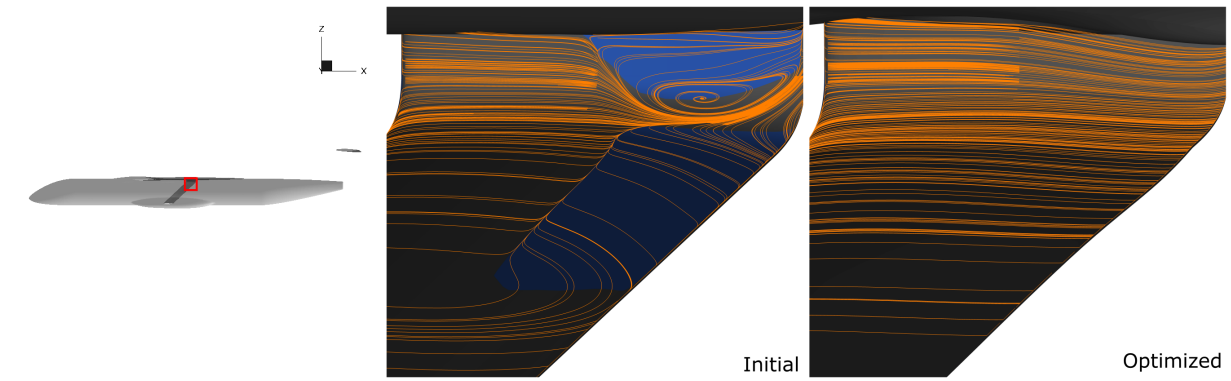

(b) Inner surface of the strut

Fig. 18 SBW100: Streamlines (orange lines) and separation contours (blue surfaces) around the wing-strut junction.

V. Conclusions

This work investigated the aerodynamic design and fuel burn performance of a strut-braced-wing regional jet aircraft based on the Embraer E190-E2, with a maximum payload of 30,200 lb, and a design range of 3,100 nmi at a maximum passenger payload of 104 PAX. The conceptual design of the strut-braced-wing aircraft was performed with a mixed low- and medium-fidelity MDO framework, assuming year 2020 technology levels, with the conceptual sizing of a conventional tube-and-wing aircraft also included to serve as a performance baseline.

Aerodynamic shape optimization was then applied to the aerodynamic design of each aircraft, with the objective of minimizing cruise drag for a nominal mission of 500 nmi at Mach 0.78. Results indicate that aerodynamic shape optimization based on the RANS equations, with the aid of a patch-based junction deformation scheme, is capable of mitigating shock formation and boundary-layer separation within the wing-strut junction, maintaining low cruise drag performance, even while subject to both lift and trim constraints, with the former at a relatively high design C_L of 0.68. Some of the aerodynamic design features that contribute to this performance are:

- A negative lifting strut near the wing-strut junction, which is compensated locally by the wing to maintain a total spanwise lift distribution that is elliptical in form
- An outwards normal force distribution within the wing-strut junction to reduce differences in local pressure between the neighboring surfaces; this is achieved in part by an outwards directed twist distribution
- Novel airfoil shapes around the wing-strut junction to alleviate the rapid acceleration of the flow, which would otherwise cause a significant decrease in local pressure that results in shock formation and boundary-layer separation
- A positive lifting strut near the strut-fuselage junction

Compared to the similarly optimized conventional tube-and-wing regional jet, the strut-braced wing offers a 12.9% higher cruise L/D. When including the impact of weight and propulsive efficiency, as well as the fuel required for takeoff, climb, descent, and landing, this provides a 7.6% savings in fuel burn over the 500 nmi mission.

Given that the strut-braced-wing regional jet must allocate a significant fraction of the nominal mission for climbing to and descending from the relatively high cruise altitudes required by the design C_L, this results in less range cruising at the fuel-efficient design point. Therefore, we can expect a further reduction in fuel consumption when operating over a longer range, which is not unusual for regional jets of this type. Operating over longer ranges also results in higher wing loadings at cruise on average, allowing the optimal C_L to be achieved at a lower altitude, further reducing fuel burn. For example, for a 1,000 nmi mission operating at the design C_L, we estimate a 10.3% savings in block fuel to first order. This also suggests that the strut-braced-wing configuration can offer larger block fuel reductions for a longer-range aircraft, such as an aircraft in the single-aisle class, where cruise fuel represents a larger fraction of the block fuel burn.

With the feasibility of designing a low drag strut-braced-wing regional jet at Mach 0.78 demonstrated, the next step

will be to investigate whether this performance can be maintained over a suitable range of cruise conditions through multipoint optimization. Other future work includes investigating the potential advantages of the strut-braced-wing configuration for the single-aisle class of aircraft, examining more closely the tradeoffs between aerodynamics and structures, as well as the merits of a truss-braced-wing configuration with one or more jury struts, through high-fidelity aerostructural optimization, and addressing the concerns surrounding the susceptibility of these wing systems to flutter.

Acknowledgments

Financial support is provided in part by the Natural Sciences and Engineering Research Council of Canada, the Queen Elizabeth II Graduate Scholarship in Science and Technology, the Ontario Graduate Scholarship, and the University of Toronto. Computations were performed on the Niagara supercomputer at the SciNet HPC Consortium. SciNet is funded by the Canada Foundation for Innovation under the auspices of Compute Canada; the Government of Ontario; the Ontario Research Fund - Research Excellence; and the University of Toronto.

References

[1] Liebeck, R. H., "Design of the Blended Wing Body Subsonic Transport," *Journal of Aircraft*, Vol. 41, No. 1, 2004, pp. 10–25. https://doi.org/10.2514/1.9084.

[2] Wolkovitch, J., "The Joined Wing: An Overview," *Journal of Aircraft*, Vol. 23, No. 3, 1986, pp. 161–178.

[3] Prandtl, L., "Induced Drag of Multiplanes," Tech. rep., NACA, March 1924. TN-182.

[4] Frediani, A., "The Prandtl Wing," *Innovative Configurations and Advanced Concepts for Future Civil Transport Aircraft*, edited by E. Torenbeek and H. Deconinck, von Karman Institute for Fluid Dynamics, 2005. VKI Lecture Series.

[5] Cavallaro, R., and Demasi, L., "Challenges, Ideas, and Innovations of Joined-Wing Configurations: A Concept from the Past, an Opportunity for the Future," *Progress in Aerospace Sciences*, Vol. 87, No. 1, 2016, pp. 1–93. https://doi.org/10.1016/j.paerosci.2016.07.002.

[6] Drela, M., "Development of the D8 Transport Configuration," *29th AIAA Applied Aerodynamics Conference*, AIAA 2011-3970, Honolulu, Hawaii, June 2011. https://doi.org/10.2514/6.2011-3970.

[7] Pfenninger, W., "Design Considerations of Large Subsonic Long Range Transport Airplanes with Low Drag Boundary Layer Suction," Tech. rep., Northrop Aircraft Incorporated, November 1954. NAI-54-800 (BLC-67).

[8] Grasmeyer, J. M., Naghshineh, A., Tetrault, P. A., Grossman, B., Haftka, R. T., Kapania, R. K., Mason, W. H., and Schetz, J. A., "Multidisciplinary Design Optimization of a Strut-Braced Wing Aircraft with Tip-Mounted Engines," Tech. rep., NASA Langley Research Center, January 1998. MAD 98-01-01.

[9] Gern, F. H., Ko, A., Sulaeman, E., Gundlach, J. F., Kapania, R. K., and Haftka, R. T., "Multidisciplinary Design Optimization of a Transonic Commercial Transport with Strut-Braced Wing," *Journal of Aircraft*, Vol. 38, No. 6, 2001, pp. 1006–1014. https://doi.org/10.2514/2.2887.

[10] Gur, O., Bhatia, M., Schetz, J. A., Mason, W. H., Kapania, R. K., and Mavris, D. N., "Design Optimization of a Truss-Braced-Wing Transonic Transport Aircraft," *Journal of Aircraft*, Vol. 47, No. 6, 2010, pp. 1907–1917. https://doi.org/10.2514/1.47546.

[11] Meadows, N. A., Schetz, J. A., Kapania, R. K., Bhatia, M., and Seber, G., "Multidisciplinary Design Optimization of Medium-Range Transonic Truss-Braced Wing Transport Aircraft," *Journal of Aircraft*, Vol. 49, No. 6, 2012, pp. 1006–1014. https://doi.org/10.2514/1.C031695.

[12] Chakraborty, I., Nam, T., Gross, J. R., Mavris, D. N., Schetz, J. A., and Kapania, R. K., "Comparative Assessment of Strut-Braced and Truss-Braced Wing Configurations Using Multidisciplinary Design Optimization," *Journal of Aircraft*, Vol. 52, No. 6, 2015, pp. 2009–2020. https://doi.org/10.2514/1.C033120.

[13] Bradley, M. K., Droney, C. K., and Allen, T. J., "Subsonic Ultra Green Aircraft Research: Phase II - Volume I - Truss Braced Wing Design Exploration," Tech. rep., NASA and Boeing Research and Technology, April 2015. NASA/CR-2015-218704.

[14] Maldonado, D., Housman, J. A., Duensing, J. C., Jensen, J. C., Kiris, C. C., Viken, S. A., Hunter, C. A., Frink, N. T., and McMillin, S. N., "Computational Simulations of a Mach 0.745 Transonic Truss-Braced Wing Design," *AIAA Scitech Forum*, AIAA 2020-1649, Orlando, Florida, January 2020. https://doi.org/10.2514/6.2020-1649.

[15] Harrison, N. A., Beyar, M. D., Dickey, E. D., Hoffman, K., Gatlin, G. M., and Viken, S. A., "Development of an Efficient Mach = 0.80 Transonic Truss-Braced Wing Aircraft," *AIAA Scitech Forum*, AIAA 2020-0011, Orlando, Florida, January 2020. https://doi.org/10.2514/6.2020-0011.

[16] Maldonado, D., Housman, J. A., Piotrowski, M. G. H., Kiris, C. C., Hunter, C. A., Viken, S. A., McMillin, S. N., and Milholen, W. E., "Improvements in Simulating a Mach 0.80 Transonic Truss-Braced Wing Configuration using the Spalart-Allmaras and k-omega SST Turbulence Models," *AIAA Scitech Forum*, AIAA 2021-1531, Virtual Event, January 2021. https://doi.org/10.2514/6.2021-1531.

[17] Ko, A., Mason, W. H., and Grossman, B., "Transonic Aerodynamics of a Wing/Pylon/Strut Juncture," *21st AIAA Applied Aerodynamics Conference*, AIAA 2003-4062, Orlando, FL, June 2003. https://doi.org/10.2514/6.2016-3904.

[18] Bieler, H., Bier, N., Bugeda, G., Periaux, J., Redondo, D., Guttila, S., and Pons, J., "A Common Platform for Validation of Aircraft Drag Reduction Technologies," retrieved on 1 May 2018. URL http://congress.cimne.com/padri-2017/frontal/default.asp.

[19] Turriziani, R. Y., Lovell, W. A., Martin, G. L., Price, J. E., Swanson, E. E., and Washburn, G. F., "Preliminary Design Characteristics of a Subsonic Business Jet Concept Employing an Aspect Ratio 25 Strut-Braced Wing," Tech. rep., NASA, October 1980. NASA-CR-159361.

[20] Gagnon, H., and Zingg, D. W., "Euler-Equation-Based Drag Minimization of Unconventional Aircraft," *Journal of Aircraft*, Vol. 53, No. 5, 2016, pp. 1361–1371. https://doi.org/10.2514/1.C033591.

[21] Secco, N. R., and Martins, J. R. R. A., "RANS-Based Aerodynamic Shape Optimization of a Strut-Braced Wing with Overset Meshes," *Journal of Aircraft*, Vol. 56, No. 1, 2019, pp. 217–227. https://doi.org/10.2514/1.C034934.

[22] Brooks, T. R., Kenway, G. K. W., and Martins, J. R. R. A., "Benchmark Aerostructural Models for the Study of Transonic Aircraft Wings," *Journal of Aircraft*, Vol. 56, No. 7, 2018, pp. 2840–2855. https://doi.org/10.2514/1.J056603.

[23] Khosravi, S., and Zingg, D. W., "Aerostructural Perspective on Winglets," *Journal of Aircraft*, Vol. 54, No. 3, 2017, pp. 1121–1138. https://doi.org/10.2514/1.C033914.

[24] Brooks, T. R., Martins, J. R. R. A., and Kennedy, G. J., "Aerostructural Tradeoffs for Tow-Steered Composite Wings," *Journal of Aircraft*, Vol. 57, No. 5, 2020, pp. 787–799. https://doi.org/10.2514/1.C0356993.

[25] Bartels, R. E., Funk, C. J., and Scott, R. C., "Limit-Cycle Oscillation of the Subsonic Ultra-Green Aircraft Research Truss-Braced Wing Aeroelastic Model," *Journal of Aircraft*, Vol. 54, No. 5, 2017, pp. 1605–1612. https://doi.org/10.2514/1.C034064.

[26] Opgenoord, M. M. J., Drela, M., and Willcox, K. E., "Physics-Based Low-Order Model for Transonic Flutter Prediction," *AIAA Journal*, Vol. 56, No. 4, 2018, pp. 1519–1531. https://doi.org/10.2514/1.J056710.

[27] Mallik, W., Kapania, R. K., and Schetz, J. A., "Effect of Flutter on the Multidisciplinary Design Optimization of Truss-Braced-Wing Aircraft," *Journal of Aircraft*, Vol. 52, No. 6, 2015, pp. 1858–1872. https://doi.org/10.2514/1.C033096.

[28] Jonsson, E., Mader, C. A., Martins, J. R. R. A., and Kennedy, G. J., "Computational Modeling of Flutter Constraint for High-Fidelity Aerostructural Optimization," *AIAA Scitech Forum*, AIAA 2019-2354, San Diego, California, January 2019. https://doi.org/10.2514/6.2019-2354.

[29] Lowe, B., and Zingg, D. W., "Efficient Flutter Prediction Using Reduced-Order Modeling," *AIAA Journal*, 2021. https://doi.org/10.2514/1.J060006, (In press).

[30] Silva, W. A., and Bartels, R. E., "Development of Reduced-Order Models for Aeroelastic Analysis and Flutter Prediction Using the CFL3Dv6.0 Code," *Journal of Fluids and Structures*, Vol. 19, No. 6, 2004, pp. 729–745. https://doi.org/10.1016/j.jfluidstructs.2004.03.004.

[31] Lieu, T., Farhat, C., and Lesoinne, M., "Reduced-Order Fluid/Structure Modeling of a Complete Aircraft Configuration," *Computer Methods in Applied Mechanics and Engineering*, Vol. 195, No. 41, 2006, pp. 5730–5742. https://doi.org/10.1016/j.cma.2005.08.026.

[32] Hicken, J. E., and Zingg, D. W., "Aerodynamic Optimization Algorithm with Integrated Geometry Parameterization and Mesh Movement," *AIAA Journal*, Vol. 48, No. 2, 2010, pp. 400–413. https://doi.org/10.2514/1.44033.

[33] Gagnon, H., and Zingg, D. W., "Two-Level Free-Form and Axial Deformation for Exploratory Aerodynamic Shape Optimization," *AIAA Journal*, Vol. 53, No. 7, 2015, pp. 2015–2026. https://doi.org/10.2514/1.J053575.

[34] Osusky, M., and Zingg, D. W., "Parallel Newton-Krylov-Schur Solver for the Navier-Stokes Equations Discretized Using Summation-By-Parts Operators," *AIAA Journal*, Vol. 51, No. 12, 2013, pp. 2833–2851. https://doi.org/10.2514/1.J052487.

[35] Pironneau, O., "On Optimum Design in Fluid Mechanics," *Journal of Fluid Mechanics*, Vol. 64, No. 1, 1974, pp. 97–110. https://doi.org/10.1017/S0022112074002023.

[36] Jameson, A., "Aerodynamic Design via Control Theory," *Journal of Scientific Computing*, Vol. 3, No. 3, 1998, pp. 223–260. https://doi.org/10.1007/BF01061285.

[37] Gill, P. E., Murray, W., and Saunders, M. A., "SNOPT: An SQP Algorithm for Large-Scale Constrained Optimization," *SIAM Journal on Optimization*, Vol. 14, No. 4, 2002, pp. 979–1006. https://doi.org/10.1137/S0036144504446096.

[38] Spalart, P. R., and Allmaras, S. R., "A One-Equation Turbulence Model for Aerodynamic Flows," *30th AIAA Aerospace Sciences Meeting and Exhibit*, AIAA 92-0439, Reno, Nevada, January 1992. https://doi.org/10.2514/6.1992-439.

[39] Allmaras, S. R., Johnson, F. T., and Spalart, P. R., "Modifications and Clarifications for the Implementation of the Spalart-Allmaras Turbulence Model," *7th International Conference on Computational Fluid Dynamics*, ICCFD7-1902, Big Island, Hawaii, July 2012.

[40] Spalart, P. R., "Strategies for Turbulence Modelling and Simulations," *International Journal of Heat and Fluid Flow*, Vol. 21, No. 3, 2000, pp. 252–263. https://doi.org/10.1016/S0142-727X(00)00007-2.

[41] Levy, D. W., Laflin, K. R., Tinoco, E. N., Vassberg, J. C., Mani, M., Rider, B., Rumsey, C. L., Wahls, R. A., Morrison, J. H., Brodersen, O. P., Crippa, S., Mavriplis, D. J., and Murayama, M., "Summary of Data from the Fifth Computational Fluid Dynamics Drag Prediction Workshop," *Journal of Aircraft*, Vol. 51, No. 4, 2014, pp. 1194–1213. https://doi.org/10.2514/1.C032389.

[42] Del Rey Fernández, D. C., Hicken, J. E., and Zingg, D. W., "Review of Summation-by-Parts Operators with Simultaneous Approximation Terms for the Numerical Solution of Partial Differential Equations," *Computers & Fluids*, Vol. 95, No. 22, 2014, pp. 171–196. https://doi.org/10.1016/j.compfluid.2014.02.016.

[43] Piotrowski, M. G. H., and Zingg, D. W., "Smooth Local Correlation-Based Transition Model for the Spalart-Allmaras Turbulence Model," *AIAA Journal*, Vol. 59, No. 2, 2020, pp. 474–492. https://doi.org/10.2514/1.J059784.

[44] Saad, Y., and Schultz, M. H., "GMRES: A Generalized Minimal Residual Algorithm for Solving Nonsymmetric Linear Systems," *SIAM Journal on Scientific and Statistical Computing*, Vol. 7, No. 3, 1986, pp. 856–869. https://doi.org/10.1137/0907058.

[45] Saad, Y., "A Flexible Inner-Outer Preconditioned GMRES Algorithm," *SIAM Journal on Scientific and Statistical Computing*, Vol. 14, No. 2, 1993, pp. 461–469. https://doi.org/10.1137/0914028.

[46] Saad, Y., and Sosonkina, M., "Distributed Schur Complement Techniques for General Sparse Linear Systems," *SIAM Journal on Scientific and Statistical Computing*, Vol. 21, No. 4, 1999, pp. 1337–1357. https://doi.org/10.1137/S1064827597328996.

[47] Osusky, M., Boom, P. D., and Zingg, D. W., "Results from the Fifth AIAA Drag Prediction Workshop Obtained with a Parallel Newton-Krylov-Schur Flow Solver Discretized using Summation-By-Parts Operators," *31st AIAA Applied Aerodynamics Conference*, AIAA 2013-2511, San Diego, CA, June 2013. https://doi.org/10.2514/6.2013-2511.

[48] Squire, W., and Trapp, G., "Using Complex Variables to Estimate Derivatives of Real Functions," *SIAM Review*, Vol. 40, No. 1, 1998, pp. 110–112. https://doi.org/10.1137/S003614459631241X.

[49] Osusky, L., Buckley, H. P., Reist, T. A., and Zingg, D. W., "Drag Minimization Based on the Navier-Stokes Equations Using a Newton-Krylov Approach," *AIAA Journal*, Vol. 53, No. 6, 2015, pp. 1555–1577. https://doi.org/10.2514/1.J053457.

[50] Raymer, D. P., *Aircraft Design: A Conceptual Approach*, 5th ed., American Institute of Aeronautics and Astronautics, 2012.

[51] Malone, B., and Mason, W. H., "Multidisciplinary Optimization in Aircraft Design Using Analytic Technology Models," *Journal of Aircraft*, Vol. 431-438, No. 2, 1995, pp. 415–416. https://doi.org/10.2514/6.1991-3187.

[52] Torenbeek, E., *Synthesis of Subsonic Airplane Design*, Delft University, 1982.

[53] Andrews, S. A., Perez, R. E., and Wowk, D., "Wing Weight Model for Conceptual Design of Nonplanar Configurations," *Aerospace Science and Technology*, Vol. 43, No. 1, 2015, pp. 51–62. https://doi.org/10.1016/J.AST.2015.02.011.

[54] Gallman, J. W., Smith, S. C., and Kroo, I. M., "Optimization of Joined-Wing Aircraft," *Journal of Aircraft*, Vol. 30, No. 6, 1993, pp. 897–905. https://doi.org/10.2514/3.46432.

[55] Turner, M. J., Clough, R. W., Martin, H. C., and Topp, L. J., "Stiffness and Deflection Analysis of Complex Structures," *Journal of Aeronautical Sciences*, Vol. 23, No. 9, 1956, pp. 805–854. https://doi.org/10.2514/8.3664.

[56] Przemieniecki, J. S., *Theory of Matrix Structural Analysis*, Dover, 1968.

[57] Gur, O., Bhatia, M., Mason, W. H., Schetz, J. A., Kapania, R. K., and Nam, T., "Development of Framework for Truss-Braced Wing Conceptual MDO," *51st AIAA Structures, Structural Dynamics, and Materials Conference*, AIAA 2010-2754, Orlando, Florida, April 2010. https://doi.org/10.2514/6.2010-2754.

[58] Kroo, I., and Shevell, R., "Aircraft Design, Synthesis and Analysis," retrieved on 23 December 2016. URL http://adg.stanford.edu/aa241/AircraftDesign.html.

[59] Williams, J. E., and Vukelich, S. R., "The USAF Stability and Control Digital DATCOM - Volume II - Implementation of Datcom Methods," Tech. rep., McDonnell Douglas Astronautics Company, April 1979. AFFDL-TR-79-3032.

[60] "Type-Certificate Data Sheet for PW1500G Series Engines," Tech. rep., European Union Aviation Safety Agency, March 2019. No. IM.E.090.

[61] Embraer S.A., *E-Jets E2 Airport Planning Manual*, 2017. Revision 12 - 08 February 2019.

[62] Jemitola, P., "Wing Mass Estimation Algorithm for Medium Range Box Wing Aircraft," *The Aeronautical Journal*, Vol. 117, No. 1188, 2013, p. 329340. https://doi.org/10.1017/S0001924000008022.

[63] Shortal, J. A., and Maggin, B., "Effect of Sweepback and Aspect Ratio on Longitudinal Stability Characteristics of Wings at Low Speeds," Tech. rep., National Advisory Committee for Aeronautics, July 1946. NACA TN-1093.

[64] Airbus Canada Limited Partnership, *A220-300 Airport Planning Publication APP*, 2020. Issue 22 - 17 September 2020.

[65] Vassberg, J. C., Tinoco, E. N., Mani, M., Rider, B., Zickuhr, T., Levy, D. W., Brodersen, O. P., Eisfeld, B., Crippa, S., Wahls, R. A., Morrison, J. H., Mavriplis, D. J., and Murayama, M., "Summary of the Fourth AIAA Computational Fluid Dynamics Drag Prediction Workshop," *Journal of Aircraft*, Vol. 51, No. 4, 2014, pp. 1070–1089. https://doi.org/10.2514/1.C032418.

[66] Kreisselmeier, G., and Steinhauser, R., "Systematic Control Design by Optimizing a Vector Performance Index," *International Federation of Active Controls Symposium on Computer-Aided Design of Control Systems*, Zurich, Switzerland, August 1979. https://doi.org/10.1016/S1474-6670(17)65584-8.

[67] Hicken, J., and Zingg, D. W., "An Investigation of Induced Drag Minimization Using a Newton-Krylov Algorithm," *12th AIAA/ISSMO Multidisciplinary Analysis and Optimization Conference*, AIAA 2008-5807, Victoria, British Columbia, September 2008. https://doi.org/10.2514/6.2008-5807.

[68] Lovely, D., and Haimes, R., "Shock Detection from Computational Fluid Dynamics Results," *14th Computational Fluid Dynamics Conference*, AIAA 99-3285, Norfolk, Virginia, November 1999. https://doi.org/10.2514/6.1999-3285.

[69] Nemec, M., Zingg, D. W., and Pulliam, T. H., "Multipoint and Multi-Objective Aerodynamic Shape Optimization," *AIAA Journal*, Vol. 42, No. 6, 2004, pp. 1057–1065. https://doi.org/10.2514/1.10415.

[70] Demasi, L., Monegato, G., Cavallaro, R., and Rybarczyk, R., "Minimum Induced Drag Conditions for Truss-Braced Wings," *AIAA Journal*, Vol. 56, No. 12, 2018, pp. 4669–4684. https://doi.org/10.2514/1.J057225.